HOCHSCHULE RUHR WEST
UNIVERSITY OF APPLIED SCIENCES

INSTITUT
MESS-UND SENSORTECHNIK

Bachelor's thesis

Jonas Gillner

Development of a low-cost radar-based sensor system for passenger detection in automotive applications

Examination for the degree Bachelor of Science
in Automotive Electrical Engineering and Electromobility

at Ruhr West University of Applied Sciences
Department Measurement and Sensor Technology

December 4th, 2023

Prof. Dr. Klaus Thelen
Fabian Ströder, M.Sc.

Declaration of authorship

I hereby confirm that this thesis submitted on December 4th, 2023 with the title

Development of a low-cost radar-based sensor system for passenger detection in automotive applications

and the work presented in it is entirely my own. Where I have consulted the work of others this is always clearly stated. All statements taken literally from other writings or referred to by analogy are marked and the source is always given. This paper has not yet been submitted to another examination office, either in the same or similar form.

Essen, December 4, 2023
Jonas Gillner

Abstract

In this scientific research, an innovative sensor system is developed to prevent child heatstrokes in vehicles. The system incorporates a 24 GHz Continuous-Wave (CW) radar system, which identifies vital signs of an infant through a 4-by-1 patch antenna array embedded in a specifically designed circuit board. Intelligent signal processing algorithms analyze data generated by the radar chip and execute processing tasks on a robust microcontroller. The child's respiration rate can be extracted qualitatively from the data in nearly real-time, enabling the system to differentiate between a child and a mere shopping bag on the seat. In the event of identifying a critical condition, the system transmits this information via a data bus to a central ECU within the vehicle. This ECU is integrated with GSM and GPS connections, allowing communication with the driver or emergency services. The development of the sensor system adheres to existing automotive industry standards, featuring a cost-effective design intended as a prototype for large-scale production. Through rigorous evaluation across various scenarios, including real-world situations with children, the sensor system is refined. The continuously reliable function of the developed radar-based sensor system holds the potential to save children's lives, making a major contribution to automotive safety.

Contents

1 Introduction

Each year, an average of 38 infants die from pediatric vehicular heatstroke after being left unattended in a vehicle. This is caused by prolonged exposure to high temperatures, which can quickly raise the body's core temperature to over 40 degree Celsius. In the year 2022, the United States alone witnessed 28 fatalities attributed to such incidents. Given the persistent risk of this tragedy, the United States is enforcing a mandate for the integration of a system with the capability to detect and potentially prevent the abandonment of children in vehicles. Similarly, car manufacturers in the European Union are facing increased pressure to adopt similar preventive systems. [1, 2]

This research work aims to develop a cost-effective prototype radar-based sensor system, addressing the challenge and potentially paving the way for widespread adoption in the automotive industry. The sensor system is designed to detect the presence of a child by monitoring their vital signs without direct physical contact. It can detect potential overheating or the onset of frostbite, as the radar is capable of sensing the child's breathing even through layers such as blankets or jackets. Upon successful detection, immediate preventive measures are activated to rescue the child from this critical situation. The age group most susceptible to harm compromises newborn and very young infants, given their limited ability to communicate and extricate themselves from danger. Consequently, this research focuses on and promotes advancements in automotive safety, aiming to enhance protection for vehicle occupants and ultimately contributing to saving more lives.

The main objective of this scientific work is to ensure that the developed radar-based sensor system can detect the presence of a living being, specifically defined as a newborn infant up to six years of age according to [3], and distinguish it from an inanimate object situated in the passenger seat of a vehicle. The first step involves identifying a radar chip that aligns with the specific requirements of the application while being cost-effective for automotive use. Subsequently, a phased array antenna must be designed to conform to the chip's specifications. The system should encompass signal processing and analysis capabilities compatible with the radar chip, along with meeting other requirements of an automotive control unit. The next steps involve designing, assembling and commissioning a printed circuit board (PCB) for the developed system design. Following this, a crucial aspect of this system is the development of a software algorithm for infant detection. This algorithm reads and analyzes processed signals, enabling the system to determine the presence or absence of a child. The decision-making process utilizes radar signals to measure the object's distance. The system then analyzes the measurement signal for respiratory frequencies, aiding in the decision on whether the vehicle seat is occupied by a baby or infant. The complete system, comprising both hardware and software components, will undergo thorough testing to ensure its effectiveness for the intended application and ensure compatibility with automotive standards. Furthermore, measurements and characterization of the patch antenna array on the PCB will be conducted. Ultimately, based on the measurement

results, a proposal for further improvements to the system should be provided.

This thesis is structured into eight chapters, with the introductory section being the first. Chapter 2 provides an overview of the fundamental concepts of the topic to assist the reader in attaining a better understanding of the subject matter. In Chapter 3, currently available technologies are presented, differentiating the author's work from prior related research. The specific methodology employed to achieve the thesis objectives, as outlined in Section 1, is discussed in Section 4. Section 5 discusses the development of the sensor system, followed by its evaluation and analysis through tests and examination in Section 6. Finally, the findings and conclusions derived from this evaluation are presented in Chapter 7, and Section 8 summarizes the results while suggesting possible future avenues for research.

2 Basic knowledge

This chapter explains some fundamentals that are necessary for a deeper understanding of the thesis. First, the chapter provides an overview of radar technology, followed by a description of reflection and transmission and an explanation of radio frequency (RF) applications. These topics are directly relevant to the thesis and are referenced in other chapters.

2.1 Basics of radar

RADAR originated from the term "Radio Detection and Ranging" and made its technological breakthrough during World War II. Its greatest benefit is the ability to operate without the need for light or a clear line of sight. As a result, radar frequently used in scenarios where cameras or similar equipment are incapable of functioning. [4]

There are various types of radar that include simple pulse radar, continuous wave radar, and frequency modulated continuous wave radar. A pulse radar produces short-duration individual carrier pulses, which get reflected at the target object and then received back by the radar system as an echo after a corresponding delay. The delay can calculate the distance of an object. A formula for this can be found in [4]. This delay is referred to as the time of flight (ToF), which includes both the outward and return journey. This method is well-suited for measuring an object's distance. Moving objects are pinged at various positions by the pulse sequence to track their movement. These systems have certain disadvantages, such as distance resolution and the possibility of misinterpreting the ToF and Doppler effect. This issue tends to arise in the case of distant targets with high rates of motion. [4]

The name itself distinguishes this type of radar from the other two types. While the radar described emits individual pulses, the other two types emit a continuous signal known as a "continuous wave".

With continuous wave (CW) radar, a signal of the same frequency is consistently transmitted and reflected by an object, then received back. The variation between the two frequencies is analyzed when the transmitted and received frequencies mix, resulting in the beat frequency, also known as f_{B}. Most radar integrated circuit (IC)s directly output this frequency. No data can be obtained from the beat frequency for stationary objects, as the transmitted and received signals are identical. Due to the lack of signal differentiation, the ToF cannot be calculated. Therefore, no distance or range calculations are possible. However, once the object is in motion, the received frequency differs from the transmitted frequency for the duration of the movement. This disparity occurs due to the Doppler effect. The frequency difference between transmitted and received signals, Δf, is known as f_{D} when it pertains to the Doppler effect. A proportional relationship exists between f_{D} and motion, allowing for its analysis. [5]

The frequency modulated continuous wave (FMCW) radar continually modifies its frequency in the shape of a triangular or saw-tooth waveform, providing a signal different from the transmitted one. This permits distance measurement based on transit time. Nonetheless, frequency shift and Doppler effect occur in a moving object as well. a signal that is not only time-delayed, but also frequency-shifted. To distinguish between these phenomena, the FMCW radar must use triangular modulation. Figure 2.1 illustrates that the signal experiences a different frequency shift, Δf, during the rising ramp than during the falling ramp. The difference between Δf_1 and Δf_2 is the doubled Doppler frequency. [5]

$$f_{\mathrm{D}} = \frac{|\Delta f_1 - \Delta f_2|}{2} \tag{2.1}$$

By halving the difference the pure Doppler frequency can be determined in formula 2.1. To calculate the frequency shift caused by propagation delay, simply add the two shifts Δf_1 and Δf_2 shown in formula 2.2, and divide by two. [5]

$$\Delta f = \frac{\Delta f_1 + \Delta f_2}{2} \tag{2.2}$$

With these modified calculations, it is now feasible to calculate both the Doppler shift associated with the object's motion and the transit time to the object. The target's distance can be determined through frequency shift analysis. [5]

$$R = \frac{\Delta f \cdot \mathrm{c}}{2 \cdot S} \tag{2.3}$$

Apply formula 2.3 to calculate the ranging R, utilizing the speed of light c, gradient of frequency shift S, and previously calculated frequency shift value Δf. [6, 7]

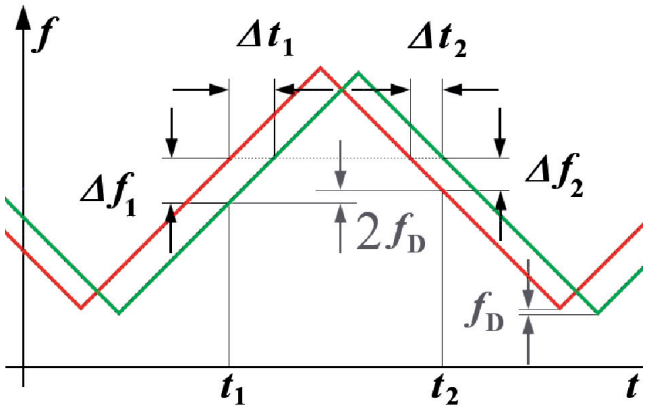

Figure 2.1: Illustration of the FMCW radar principle, adapted from [5]

2.2 Reflection and transmission

The Transmission Line Theory is a well-known concept in radio frequency technology, which deals with signal wave behavior and the resulting effects on a transmission line. Specifically, the terms transmission and reflection are particularly relevant in the design of radio frequency applications. Transmission refers to the amount of signal that reaches the target, while reflection describes the signal that is not transmitted and is instead redirected back to its source. The reflection of a two-port system can be described by the reflection coefficient Γ. This is calculated using formula 2.4 and the normalized load impedance $Z_{\mathrm{nL}} = \frac{Z_{\mathrm{L}}}{Z_0}$. [8]

$$\Gamma = \frac{Z_{\mathrm{nL}} - 1}{Z_{\mathrm{nL}} + 1} \tag{2.4}$$

Nowadays, scattering parameters are commonly used for representation due to their ability to relate to both reflection and transmission. [8]

$$S = \begin{pmatrix} s_{11} & s_{12} \\ s_{21} & s_{22} \end{pmatrix} \tag{2.5}$$

These parameters are housed in the 2×2 matrix S (see 2.5), with s11 and s22 describing the reflection as they refer from port 1 to port 1 and from port 2 to port 2. The parameters s12 and s21 refer to transmission, measured between port 1 and port 2, and between port 2 and port 1, respectively. In a linear system, these parameters can be mirrored on the main matrix diagonal, so that $s_{11} = s_{22}$ and $s_{12} = s_{21}$. This allows for the design to be optimized to minimize reflection and maintain undisturbed transmission. [8]

2.3 Patch antenna arrays

Patch antennas gained popularity due to the minimized microwave circuits in cell phones, aerospace engineering, and the automotive industry. These antennas are frequently utilized in cases where system dimensions, weight, and expenses are crucial parameters. Such aspects become increasingly significant in mass production, where pricing per unit and effectiveness, partly reliant on weight, shape the forthcoming transportation industry. Additionally, patch antennas offer the advantage of ease of mass production and reproducibility. The required longevity in the automotive industry is achieved through the mechanical resistance of the patch antenna structure, eliminating the need for changes. [9]

However, the design comes with drawbacks such as low bandwidth and an inevitable loss in the substrate. The substrate, with height h, is placed under the conductive metal of the patch antenna, with height t. Material selection is critical due to losses in the development of patch

antenna. The substrate requires a stable relative permittivity ϵ_r across a wide frequency range. The substrate is located over a ground plate of thickness t_GND. Patch antennas can take rectangular, circular, diamond-shaped, triangular, or linear forms. This thesis examines rectangular patch antennas, which function as microstrip line (MSL) open on all four sides. The wave propagation on a patch is not straightforward, requiring the use of empirical approximation formulas. However, developing the antenna is a complex process due to the need for detailed calculations, which can quickly become convoluted.

The optimal length of the patch should be chosen to achieve half-wave resonance along the shape and a real input impedance $Z_\mathrm{E} = R_\mathrm{E}$ for minimal losses from reflections. Two common ways to feed the patch antenna are through a coaxial line from beneath the substrate or a MSL on the antenna's side. Other feeds are not pertinent to this work and can be found in source [X]. The location of the feed point on the patch, specified by its coordinates x_s and y_s, is just as crucial as the type of feed used [9]. This is due to the need for impedance matching, as the impedance is $0\,\Omega$ at the center of the patch and is infinite in the corners theoretically, but in practice it has an impedance between 200-400 Ω. Therefore, if the feed point is optimally positioned to match the feeding network impedance, no additional matching network would be necessary for the feeding MSL. [5]

Calculating the length L and the feed point is a multi-step process. Begin by calculating the width W.

$$W = \sqrt{\frac{h \cdot \lambda_0}{\sqrt{\epsilon_\mathrm{r}}}} \cdot \left[\ln\left(\frac{\lambda_0}{h \cdot \sqrt{\epsilon_\mathrm{r}}}\right) - 1\right] \tag{2.6}$$

The calculation of formula 2.6 utilizes the established values of the patch antenna and the wavelength in vacuum λ_0, where c denotes the speed of light and f represents the frequency. [9]

$$\lambda_0 = \frac{c}{f} \tag{2.7}$$

To determine the length L and coordinates x_s and y_s of the feed point with calculated width W, a set of complex calculations is required. These calculations can be referenced in source [9], and formula 2.8 can then be applied to obtain the length L.

$$L = \frac{\lambda_0}{2 \cdot \sqrt{\epsilon_\mathrm{r,eff}}} - 2 \cdot \Delta L \tag{2.8}$$

$\epsilon_\mathrm{r,eff}$ and ΔL must be computed through calculations in source [9]. Formula 2.9 applies to the x-coordinate x_s of the feed point, which corresponds to the length L. [9]

$$x_\mathrm{s} = \frac{\lambda_0}{2 \cdot \sqrt{\epsilon_{\mathrm{r,eff}}} \cdot \pi} \arccos \sqrt{2 \cdot G_\mathrm{r} \cdot R_\mathrm{E}} - \Delta L \tag{2.9}$$

The input impedance required for the feeding network is denoted as R_E, and G_r is calculated from source [9]. The y-coordinate y_s of the feed point in Formula 2.10 is easily calculated as it is based on the width W and located at the center of the patch. [9]

$$y_\mathrm{s} = \frac{W}{2} \tag{2.10}$$

Once all these calculations are complete, the patch antenna parameters can be determined entirely.

The patch antenna is inflexible and cannot align its main lobe with sufficient concentration as necessary. Additionally, the radiated concentration of the patch antenna does not meet the requirements of automotive applications. Patch antenna arrays are employed to achieve the desired results. This is achieved by combining multiple planar single radiators into arrays, focusing the antenna beam like a lens. Increasing the amount of patches in a linear direction causes a more concentrated main lobe and fewer side lobes. It is crucial to reduce the side lobes to $-13\,\mathrm{dB}$ in comparison to the main lobe to prevent false target detection. The spacing between each grouped individual lobe typically ranges from $\lambda_0/4$ to λ_0. With advanced technology, the narrowest beams can be produced with exceptionally low side lobe values, resulting in a decrease in the number of false detections. [9, 10]

Antenna arrays have the advantage of being able to move the beam via amplitude and phase modulation without any mechanical movement, achieving the same results as a rotating antenna. This is especially useful in scenarios where the radar needs to reach different positions, minimizing false detections. [5]

2.4 Microstrip line feeding network

The antenna array is fed via a microstrip feeding network. The design of the feeding network is crucial for how the individual patches are fed. Two methods are used - series feeding and parallel feeding. For arrays with multiple patches in both x and y directions, a parallel and serial connection combination can be employed. [9]

In series feeding, the phase difference between adjacent pads affects the main lobe. As a result, the main lobe is no longer vertically positioned on the structure, but instead tilted by the swivel angle on the circuit board. This is not the case with a structure fed in parallel. Consequently, it behaves as a transverse radiator with a swivel angle of zero, unless there is amplitude or phase modulation to move the main lobe. [9]

Figure 2.2: Corner of a microstrip line (a), optimized with a chamfered corner (b)

When patches are fed in parallel, each antenna pad receives the signal in the same phase and power as long as it's evenly distributed in the feed network. In the parallel design, corners and crossings are emphasized to minimize reflections, whereas the serial design focuses on differences in pad sizes. Developers can consider the S1.1 parameter for this purpose. [9]

Corners in RF applications can cause issues, as a bend results in capacitance that leads to signal reflections and reduced power. Several methods exist to address this problem, including adapting the cable corners. Chamfering the corner with a specific ratio is the most effective solution.

$$b = 100 \cdot \frac{s}{d'} \tag{2.11}$$

Formula 2.11 represents the bevel b, with d indicating the MSL width (see figure 2.2). A good transmission can be achieved with a ratio of approximately $b = .7$ [11]. To achieve optimum transmission, calculate the ratio b_{opt} using formula 2.12.[12]

$$b_{\text{opt}} = 52 + 65 \cdot e^{-\frac{1.35 \cdot d}{h}} \tag{2.12}$$

The resulting bottleneck and removed corner compensate for the capacitance. In the RF technique, a bottleneck always has an inductance. Thus, it's crucial to adjust the ratio S optimally. If the chamfer is excessively large, the corner can also exhibit an inductive effect. [12]

T-junctions and corners require equal attention. The signal should be split precisely at a T-junction to avoid asynchrony. Various recommended construction methods are available and can be found in source [11] with building instructions.

2.5 Representation of I&Q-values

Displaying signals with in-phase and quadrature components is a simple way to determine the phase of an unknown sinusoidal signal. Recording the frequency of a phase-shifted sinusoidal signal is a straightforward process. The challenging aspect is detecting the phase due to its periodic nature. As demonstrated in the formula 2.13, a sinusoid with a phase shift can be divided into two zero-phase sinusoids with amplitudes. Fortunately, detecting the amplitude of a sine wave is simple. Using this method, the amplitude component of the cosine part serves as the Real component, representing the in-phase value of the signal. The sine component's amplitude in formula 2.13 will signify the imaginary part, or quadrature value, of the sinusoid.

$$A \cdot \cos(2\pi f t + \phi) = A \cdot \cos(\phi) \cdot \cos(2\pi f t) - A \cdot \sin(\phi) \cdot \sin(2\pi f t) \tag{2.13}$$

The I-signal is the in-phase part, while the Q-signal is the quadrature part. The formula 2.14 can be used to obtain the absolute amplitude of the sinusoid.

$$A = \sqrt{I^2 + Q^2} = \sqrt{(A \cdot \cos(\phi))^2 + (A \cdot \sin(\phi))^2} \tag{2.14}$$

To obtain the phase angle, use the arctangent two (atan2) function with the quotient of I and Q.

$$\phi = \text{atan2}(Q, I) \tag{2.15}$$

The phase of the sinusoid represented by the I&Q-values can be determined by using formula 2.15. This method is frequently used for representing the beat frequency f_B in radar technology.

3 State of the art

A child presence detection sensor system must be installed in all newly registered vehicle types by 2025 [2]. This is because of the reported deaths of children due to heatstroke, as stated in Chapter 1. Different organizations such as the European New Car Assessment Program (NCAP) are dedicated to standardizing this initiative. The NCAP has released a "Test and Assessment Protocol" for child presence detection. The protocol presents the sensor system specifications evaluated by the organization for developed systems.

The standard differentiates between direct sensing and indirect sensing, where indirect sensing can only detect the potential presence of a subject in the car but cannot distinguish between living beings and inanimate objects, as it relies on sensors such as door sensors or pressure and capacity sensors. Direct sensors are able to detect a person inside a vehicle. Consistency in detecting vital signs helps in determining if a person is inside the vehicle. To achieve this, the sensor must detect vital signs like heartbeat or breathing. Additionally, movement or similar signs of life can also be used in this detection method. [3]

Warning methods for direct sensors include initial and escalation warnings. The initial warning indicates to the driver, by way of external signal, that a child may be stuck inside the vehicle. This warning is triggered by direct or indirect sensing and, as of 2025, must include both an audible and visual signal. The escalation warning, generated by direct sensing, involves a permanent or recurring notification to the driver that a child is likely present in the vehicle. [3]

Methods of intervention are described, with the primary focus being the prompt release of the child from the vehicle. To do this, external persons have to be be notified, which can be done by the driver or the emergency service. The eCall system is recommended for this purpose. This electronic emergency call system utilizes a mobile phone and GPS connection to automatically detect accident situations with the help of sensors, making an emergency call [13]. It's been mandatory in Europe for all vehicles with new type approval since the end of March 2018 according to the EN15722 standard [14]. The Euro NCAP protocol also specifies additional support procedures. For instance, the vehicle should have the capability to be unlocked automatically or remotely by either the driver or a supervisor. Additionally, the vehicle's interior temperature needs to be lowered. To achieve this, the windows should be rolled down. [3]

The breathing rates that must be identified are also specified in the Euro NCAP protocol. These ranges from 30 beats per minute (bpm) for a newborn to 18 bpm for a six-year-old. As explained in chapter 1, it is important to detect children within these age limits because they are the most vulnerable. [3]

Several systems have been studied to address the issue of heatstroke in children left in vehicles. In the past, these systems have used door contact sensors, force sensors, or capacitive sensors. Door contact sensors track the rear door opening sequence and, in some cases, alert the driver when

leaving the vehicle if a child has been left behind. Existing systems such as "Rear Door Alert" at Nissan and General Motors, and "Rear Occupancy Alert" at Hyundai. Force or capacitive sensors can detect the presence of an object on the seat. If the driver leaves the vehicle and the seat is occupied, appropriate service can be provided. However, this system has a drawback of also triggering an alarm for non-living objects like a shopping bag, making it impossible to differentiate between a child or an object left behind. [2] Therefore, the emphasis is on sensors that meet the criteria for the vital sign direct sensing system. Furthermore, research is underway on older sensor technologies. A study conducted by Source [2] presents a project that identifies breathing frequency using force sensors. To distribute the weight of the child uniformly, a minimum of four force sensors are positioned beneath the seat. If a baby is breathing in this seat, the sensors detect a change in force distribution from front to back. The breathing rate is extracted from this differential signal during analysis. The car owner is then alerted by a text message and app through a Global System for Mobile Communication (GSM) module in the control unit, which also provides current coordinates.

Nevertheless, the industry's main focus currently lies on RF sensors. The company Marquardt has already developed such a system. It uses ultra-wideband (UBW) technology and artificial intelligence (AI) to recognize the vital signs of a child in the car. By analyzing the data with the AI, it is even possible to make statements about the state of health and age of the infant detected. The radiation from the radar system does not affect the health of the children. During development, the system has already been tested with a hundred children between the ages of 0 and 10 and the AI has been trained with their data. The Marquardt sensor system is placed in each row of the vehicle for detection. It measures the flight time of the signal previously emitted and then reflected on the child. Due to the constant rise and fall of a breathing child's chest, the reflected signal shows small differences. These differences are very evenly and exhibits a specific pattern. This means that the breathing rate can be read from the signal and even assigned to a specific age using AI. This method works effectively even through thick objects like winter jackets, blankets, or child seats. [15]

Bosch and Continental are also developing systems for detecting the presence of passengers. As RF technology in cars is not new, Continental has adapted one of its existing systems. The Continental Smartphone-based Access (CoSmA) system provides a convenient way to access the car. The system allows the vehicle to be unlocked and started using a smartphone car key, provided the phone is inside the car. Therefore, this system continuously monitors the interior of the vehicle. This serves as an ideal foundation for the sensor system described and discussed in the paper, as Continental has simply integrated this feature into its existing sensor system. [16]

In addition to other research work that shares the same goal but employs differing technologies, there are industry products available. Source [17] details a radar-based sensor system that uses a patch antenna, placed anywhere in the car, to detect a child from above. The system relies on FMCW technology to measure the distance between the child and the sensor. The

technology operates at frequencies of 77 GHz to 81 GHz, achieving a 4 GHz bandwidth and a distance resolution of 3.5 cm. However, vital signs of the child cannot be detected with this technology. Future research aims to detect vital signs using radar technology. Source [18] is currently developing a radar system that can detect the respiration rate of a child using a 24GHz radar system. This research comes close to achieving the objectives of the thesis, but lacks technical details about the system. It is evident that the microcontroller used is cost-effective, but it cannot function as an independent control unit capable of performing a comprehensive data analysis. No information about the antenna used is provided. According to Source [19], child presence detection systems utilizing radar technology are not cost-effective. Therefore, a combination of research technologies that function effectively and are mass producible at a low-cost is not available.

4 Methodology

This chapter discusses the methodology employed to achieve the objectives outlined in Section 1. The design of the PCB serves as the cornerstone for this methodology. A radar IC capable of CW and FMCW operating modes, is selected, as explained in Chapter 2.1. This choice is made to facilitate the detection of breathing in a child, as discussed in Section 3. Following the selection of the IC, specifying the frequency range, the design of the patch antenna array is detailed in Section 5.1.2, taking into account the PCB specifications. Maintaining consistent adherence to metrics and units is essential for precision in the design process. Similar to the approach outlined in Chapter3, a suitable PCB substrate material is used for the high-frequency PCB. The choice of a manufacturer for antenna production is based on acquired information. However, the design process is only briefly discussed as it is a partial aspect of the main objective. Instead, a suitable simulation tool, such as Antenna Magus and CST Studio Suite, is chosen for antenna design and simulation. CST Studio Suite, a 3D simulation program designed for high-frequency electromagnetic applications and systems, is selected. Antenna Magus, a subprogram of CST, facilitates antenna design and export to CST. The software is utilized to design and optimize the antenna in accordance with the mathematical principles outlined in Chapter 2.3 to meet the specified objectives.

In addition to detailing the RF part design, Section 5.2 provides an overview of the entire sensor system circuitry. The system is designed to comply with automotive industry standards, ensuring a design that mimics real-world conditions. A deliberate effort is made to incorporate cost-effective components, aiming to minimize the overall cost. To align with mass production considerations, the component pricing is estimated based on the assumption of purchasing 1000 units. While this quantity falls short of the typical quantities in the automotive industry, it remains a practical approach for commercial dealers. To streamline the research process and accelerate proceedings, comparable components with similar properties are substituted utilizing the existing stock available at the research facility. This approach eliminates the necessity for extended waiting periods.

The autonomous system is required to autonomously conduct measurements and analyze data without external system interference. Another device is assigned the responsibility of alerting the driver or rescue service, with a circuit-provided bus connection available for this purpose. Given the absence of an eCall or similar control unit, as outlined in Section 3, information is presented on an LCD. When necessary, specific circuit components undergo simulation before being integrated into the PCB to ensure proper functionality. This allows the software to be pre-developed so that results can be obtained directly when the high-frequency PCB arrives. Due to the long production time of the high-frequency PCB, redesigning it within the processing time is not feasible. To determine the function of the LF circuit part, a conventional material design in addition to the high-frequency PCB is ordered.

The primary function revolves around measuring CW, which is entirely sufficient for detecting breath. The movement caused by breathing is detectable by a CW radar system, as elaborated in Chapter 3. Extracting the breathing frequency requires a signal processing algorithm, and the algorithm is developed using software outlined in [2]. To tailor the algorithm for the sensor system detailed in Section 5.4, MATLAB is employed to process recorded data from initialization measurements. Following necessary adjustments, the algorithm can be implemented and tested on the microcontroller.

Chapter 6.3 provides further evaluation of the antenna. Unfortunately, due to time constraints, this evaluation was not carried out using a network analyzer and an additional circuit board exclusively designated for the antenna. Instead, a straightforward high-frequency reflector was employed to characterize the antenna, considering the main lobe abstraction angle. This characterization can be achieved through the distance measurement in the FMCW mode.

Finally, the outcomes of testing the sensor system on a real infant are presented in Chapter 6.4, marking the accomplishment of the project's primary goal. Consistent and successful detection by the system is essential for validating its intended objective, which involves measuring the infant's breathing rate using the developed sensor system. To effectively achieve this objective, it is vital to conduct a thorough examination of each individual hardware component, coupled with an assessment of the overall integrated performance. It is essential to meticulously address and integrate each hardware component into the overall system design. Failure to comprehensively include and examine any single component may result in a deficiency in the overall functionality of the system. The interconnected nature of hardware components underscores the importance of a holistic approach to ensure the proper functioning of the entire system.

5 System design

This chapter describes the design of the system. This includes the development of the circuit, which is divided into RF and low frequency (LF) parts, the design of the PCB and the development of the software algorithm. The circuit design uses components that have been verified for the automotive sector and are inexpensive. In addition, standard E-Series sizes are used and as few different components as possible are used.

5.1 RF circuit design

In this section, the details of the RF part of the design are explained. First, the radar chip has to be chosen to define the operating frequency and the bandwidth of the system. With this, the antenna structure can be built. The MSL in the feeding network and the patches of the antenna are discussed in this section, based on the radar chip selection. These form the complete patch antenna array. The entire structure is created using the simulation program Antenna Magus from CST. It is specified in which center frequency antenna should operate, the bandwidth the antenna should fulfill, the substrate is used, and how high the substrate is in the PCB to be used. With this information, the software creates iterations of antennas and indicates to what percentage the antenna matches the given specifications. The antenna with the highest match, in this case 91 %, is selected and pre-simulated in Antenna Magus. When the results roughly fit, the antenna can be exported and adjusted and improved in the CST software. For this purpose, the corners and intersections of the MSL can be adjusted and the patches of the antenna array can be changed in terms of length, width and spacing.

5.1.1 Radar IC

The BGT24LTR11N16 radar chip from Infineon is selected due to its small size in the TSNP-16-9 package and low-cost as compared to other radar chips for these applications [20]. Infineon claims that it is mainly intended for CW applications, but it can also be utilized for FMCW applications due to the fully integrated voltage controlled oscillator (VCO). The chip works in the K-band from 24 GHz to 24.25 GHz in accordance with the IEEE standard [21], resulting in a 250 MHz bandwidth [20]. It features both a transmitting and receiving pin that can function simultaneously. Control and communication with the chip happen through analog voltages, rather than a typical bus interface. However, this is not a significant disadvantage for the intended use as the data is available in its unprocessed I&Q-values which can be analyzed. However, a low-cost application of the work requires an amplifier circuit, which increases the overall system cost by a few cents. Despite this, the chip's properties described above make it an excellent fit for achieving the work's objectives.

5.1.2 Patch antenna array design

To design the antenna, the radar IC specifications and the product properties of the PCB supplier are transferred to Antenna Magus. The selected manufacturer can create high-frequency PCBs in Rogers 4350B. This material meets the requirements stated in Section 2.3. It has a frequency-stable ϵ_r of 3.48 and a loss factor of 0.0037. According to the product sheet, the substrate height is 254 µm and the antenna's metal thickness is 35 µm, while the ground plane is 18 µm thick. Based on these specifications, a 4-by-1 patch antenna array fed in parallel ranks first in the automotive antennas created, with a 91 % match. The complete antenna structure is exported to CST and simulated, resulting in diagram 5.1 for the S1.1 parameter.

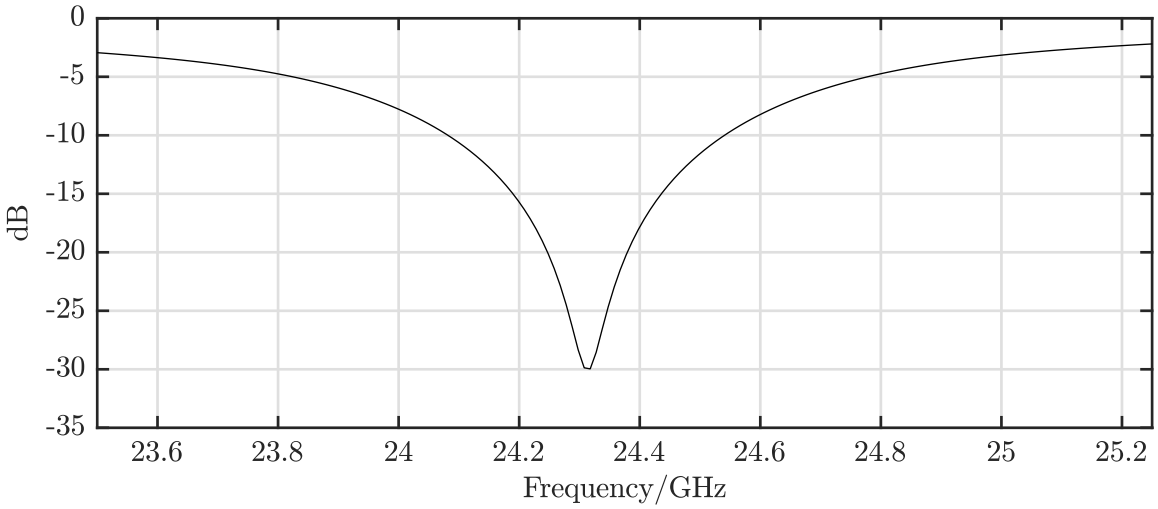

Figure 5.1: S1.1-Parameters of the antenna proposal from antenna magus

It is evident that the antenna can function within the desired range, defined as -3 dB. This indicates that approximately 50 % of the power is transmitted and the other half is reflected. However, the focus of this study is minimum -10 dB for transmitting over 90 % of the power. Additionally, the minimum reflection peak is located at around 24.3 GHz, but the goal of this project is 24.125 GHz, which is precisely the center of the operating frequency.

The formulas from chapter 2.3 are applied to each individual patch for optimization. The patch width and length are adjusted, and the feed insert point is set correctly. If the desired result is not achieved, the patch width and spacing are further optimized in CST by performing a parameter sweep and selecting the parameters that meet the target outcome.

In addition to modifying the patch, the feeding network is also analyzed, specifically the corners and junctions in the parallel feeding network. Following the information from Section 2.4, CST simulates corners and junctions separately in various designs, and the optimal design is then implemented in the feeding network.

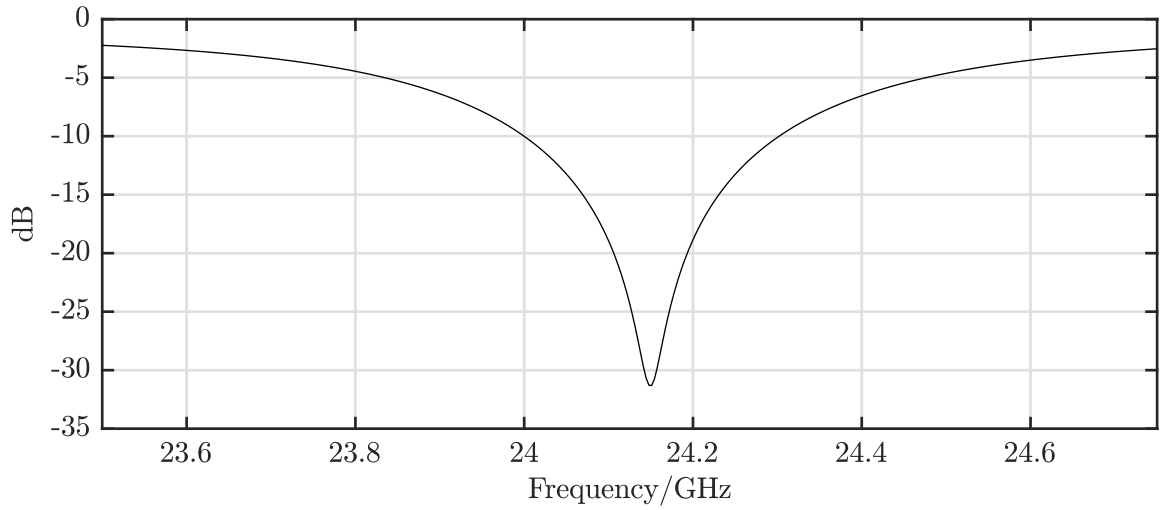

Figure 5.2: S1.1-Parameters of the final antenna

After optimizing the patches and feed network, the S1.1 parameter in diagram 5.2 indicates that the peak is now situated at the desired position between 24.125 GHz and 24.15 GHz. Furthermore, the entire operating range remains below -10 dB. As a result, the antenna structure is proved to fit the intended application of the system, signifying the success of the antenna design process with the aid of CST.

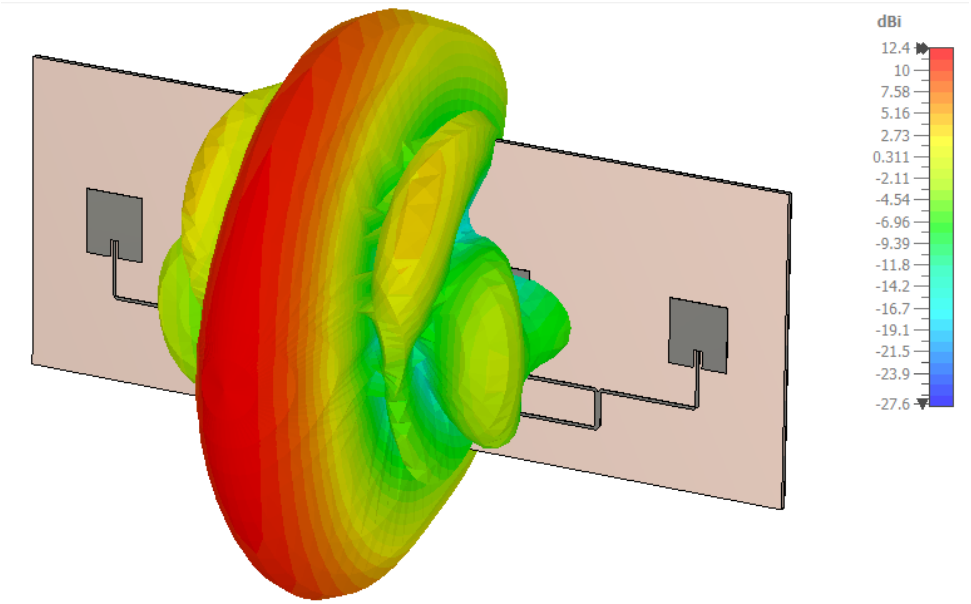

Figure 5.3: Three-dimensional far field plot of the antenna

Furthermore, Figures 5.4 and 5.5 depict the 1D far field with the radiation angles of the antenna in the horizontal and vertical planes, respectively. Figure 5.3 shows the 3-dimensional far field with a perspective view. Detailed figures of the far field can be found in A.1. The crescent shape of the antenna is highly beneficial for the intended purpose, as it enables focusing on a seat's

width while covering the entire body's height. This capability allows for easy detection of small children in various child seats. Therefore, the antenna is exported for placement on the PCB in Section 5.3.

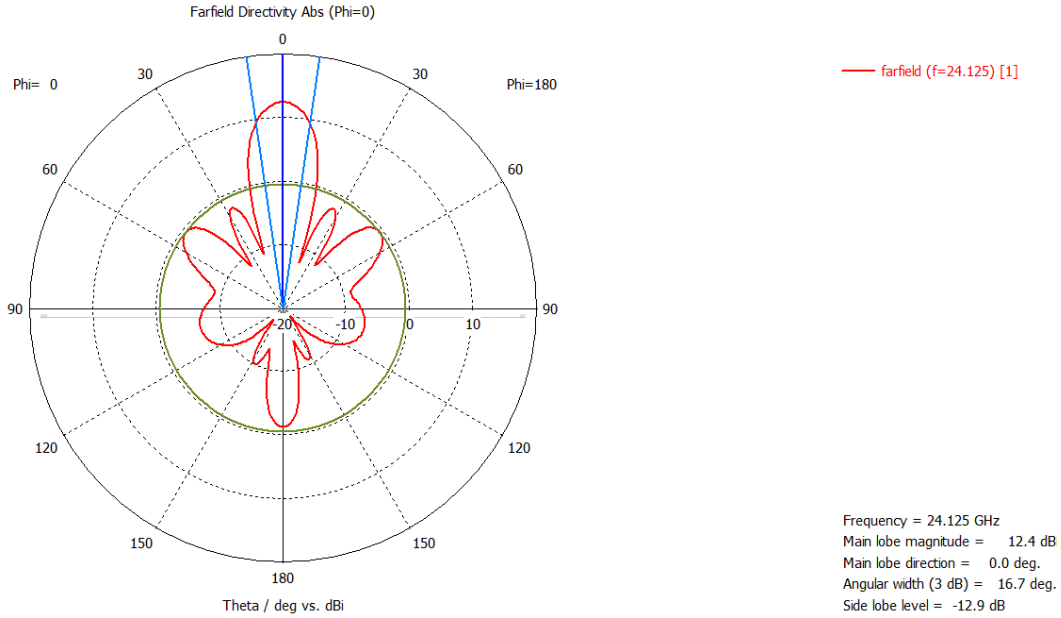

Figure 5.4: One-dimensional far field plot of the antenna observed at a 0° viewing angle

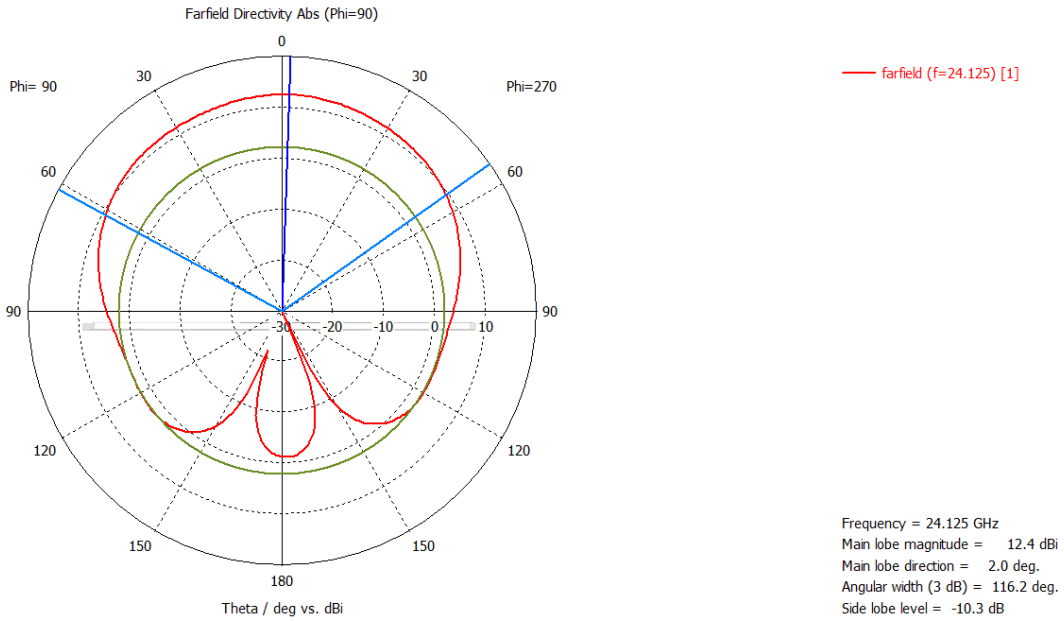

Figure 5.5: One-dimensional far field plot of the antenna observed at a 90° viewing angle

5.2 LF circuit design

The LF section of the circuit board is equally vital as the RF section. It is responsible for controlling the RF electronics as well as reading and processing output signals from the RF part. Additionally, this section meets the standard requirements for electronics used in automotive applications.

5.2.1 Amplifier stages

To utilize the analog-to-digital converter (ADC) of the microcontroller for reading the analog voltage values of the I&Q-values, an amplification necessary. An effective solution is the implementation and simulation of a two-stage amplifier circuit with various filters from [22] in LTspice. The model in Figure 5.6 clearly demonstrates the filtering out of low frequencies during the simulation. A capacitor is connected in series between the first and second amplifier stages to prevent amplification of the DC offsets of the radar chip. The simulation in Figure 5.7 presents the low gain signal in black and the high gain signal in gray. The simulations shows that lower frequencies are not amplified. While this is not a problem for standard radar applications, it is in this application. The focus of the work is the detection of a breathing frequency, which ranges from 0.25 Hz to a maximum of 1 Hz. The amplifier circuit needs modification to amplify frequencies within this range. The capacitance between the two amplifier stages cannot be removed to further prevent the amplification of the DC offset. The AC signal that is received at amplifier stage two should be characterized by half of the microcontroller's supply voltage. This enables the detection of the largest possible amplitudes. The microcontroller and a voltage divider provide the 2.5 V reference voltage. Figure 5.8 illustrates the modified simulation model.

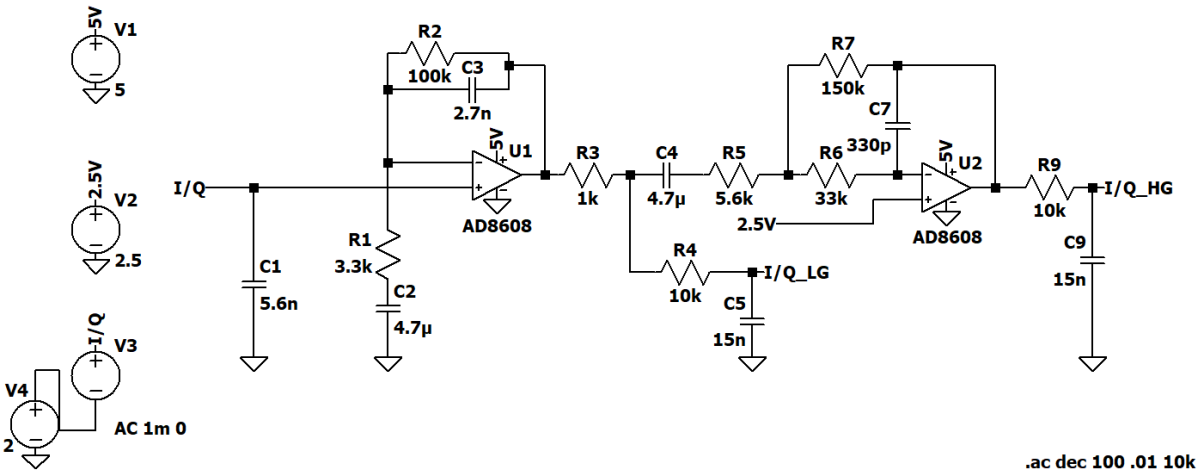

Figure 5.6: Simulation model of the given amplifier stages from [22] in LTspice

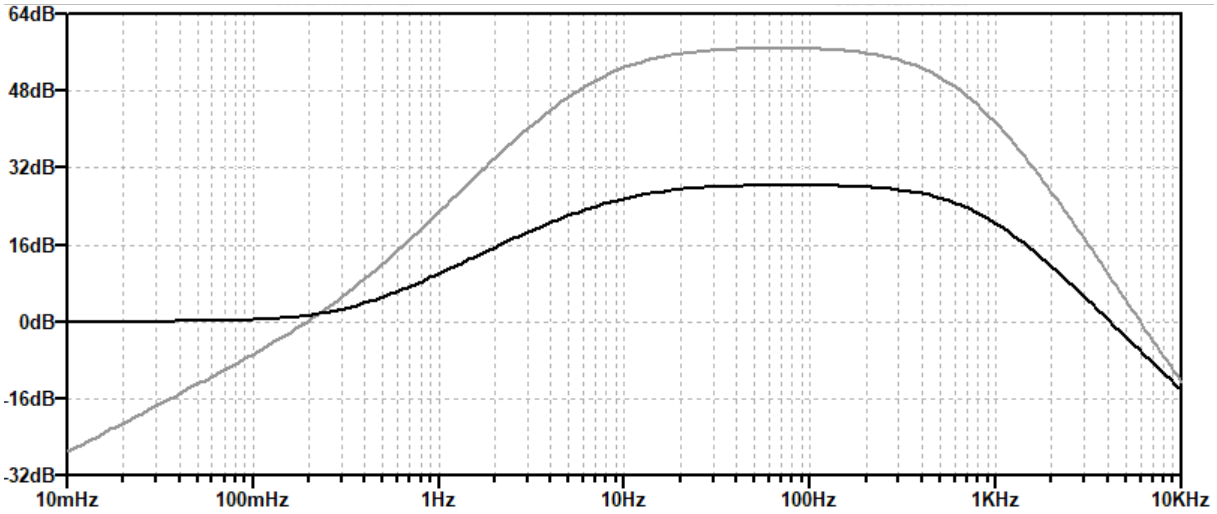

Figure 5.7: AC Analysis of the given amplifying stages from [22] in LTspice

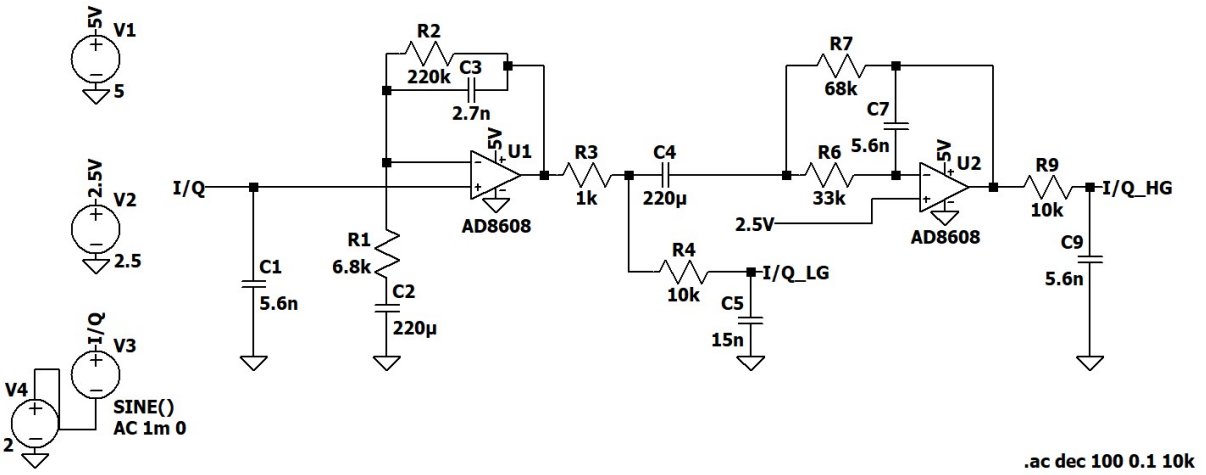

Figure 5.8: Simulation model of the adjusted amplifier stages in LTspice

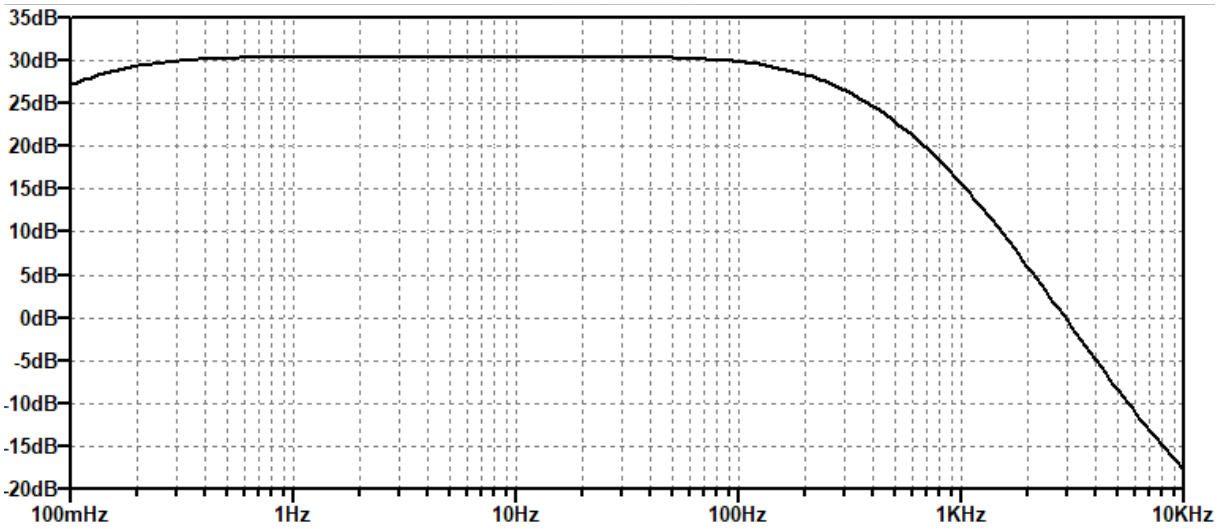

Figure 5.9: AC Analysis of the adjusted first amplifying stage in LTspice

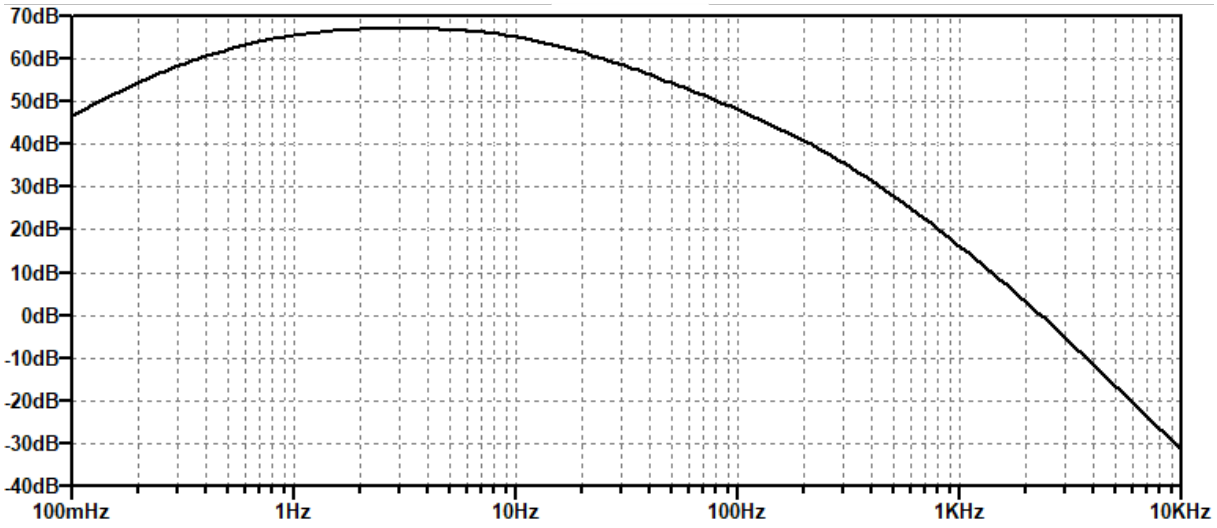

Figure 5.10: AC Analysis of the adjusted second amplifying stage in LTspice

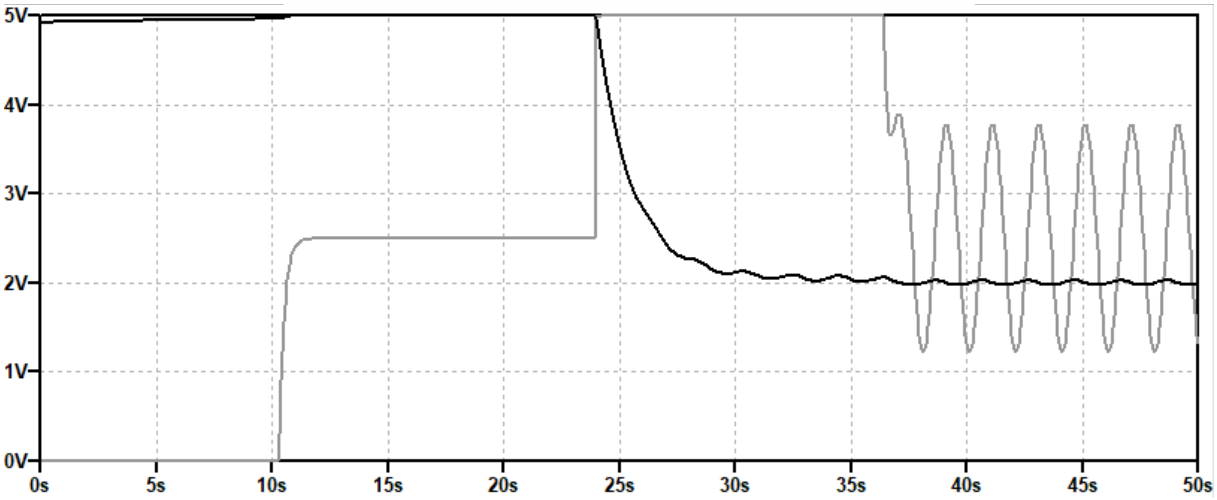

Figure 5.11: Transient behavior of the amplifying circuit in LTspice

The AC analysis results indicate the output voltage of the first and second amplifier stages in Figures 5.9 and 5.10, respectively. The figures demonstrate the successful amplification of frequencies within the desired spectrum. The simulation model is then transferred to the circuit shown in Figure 5.12. Additionally, a simulation of the time behavior is conducted. Due to the large capacitance in the circuit, the system suffers from long transient responses and is clearly visible in the simulation lasting 50 s. To meet the quiescent current requirements in the automotive industry, the system must remain switched off until the time when the measurement starts. This cannot be predicted. Accordingly, premature switch on cannot be a compensation for the transient time behavior. This issue cannot be resolved through altering the amplifier circuit, as the significant capacitance and resistance values required for the low-frequency amplification, which is previously explained. An alternative solution is the usage of small analog switches, depicted in Figure 5.13, which facilitate the switching of small analog signals. These pre-charge the large capacitors by connecting them to the output of the amplifier. This can be accomplished using Figures 5.12 and 5.13 to trace the necessary connections.

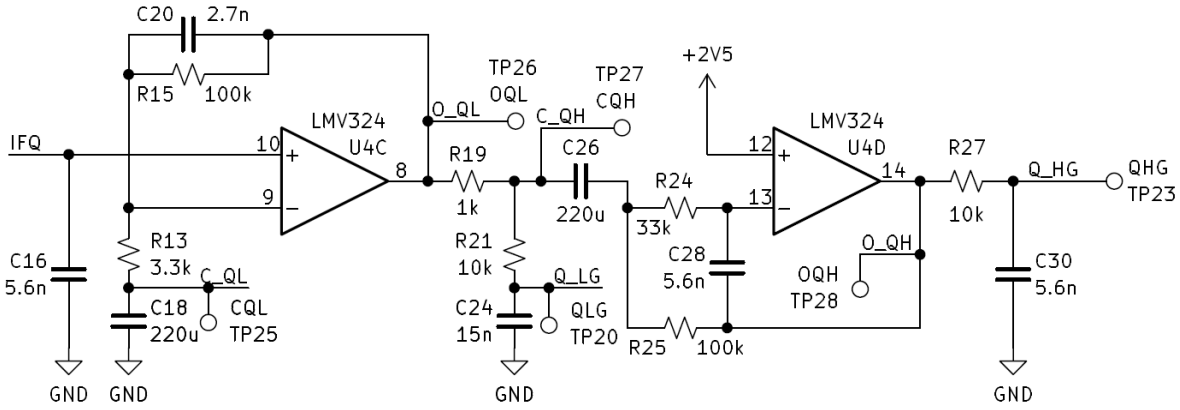

Figure 5.12: Schematic of the modified amplifying circuit for the I-signal (Q is equivalent)

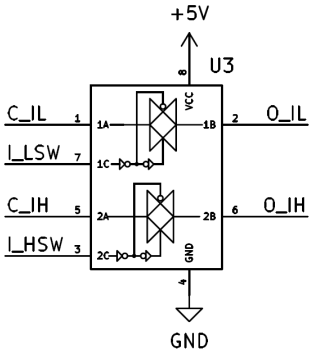

Figure 5.13: Schematic of the analog switch for the I-signal (Q is equivalent)

To accomplish this, the switches are used to short the large resistors. This creates almost an infinite steep in the charging curves of the capacitors. So, the time constant is minimized. These switches are controlled by the microcontroller of the system. When a measurement is imminent, the first amplifier stage is pre-charged for a duration of 8 ms. In this time the link between the amplifier output and the capacitor at the amplifier input is severed. After this time the amplifier is allowed to operate normally and the analog switches turn off. The second amplifier stage is pre-charged for additional 8 ms using the same principle, resulting in a total pre-charging time of 16 ms. No system operation is possible during this time. Nonetheless, this presents a noteworthy reduction in time when compared to the initial transient time of 37 s. This is an intelligent method to get allow the amplification of low frequencies and achieve a minimum settling time.

5.2.2 Microcontroller Unit and Digital-to-Analog Converter

The choice of microcontroller is vital since it handles the complete system operation and processes all signals produced. An AVR controller is preferred as it is already familiar in use and could be implemented as part of this study's software. Therefore, the Atmega1284P in the TQFP-44 package is the best choice. Operating up to 20 MHz positions it as one of the high-end models from the AVR family. The Atmega1284P is an 8-bit microcontroller with 16 kB of RAM, chosen for its ample memory required for complex signal processing in this sensor system. Most other AVR chips have insufficient RAM of 2 kB or less, making the Atmega1284P the most cost-effective solution meeting this requirement. One significant drawback is the controller's 44 pins are unnecessary and take up valuable space. However, it is the sole possibility to procure a suitable RAM while still adhering to the standard AVR family. The controller features four timers, an ADC with 8 analog inputs, and bus/serial interfaces, all of which are essential for this sensor system. The controller is programmed utilizing an ISP interface. The data is transmitted through the I^2C protocol. [23] Unfortunately, the controller does not have a digital-to-analog converter (DAC), so an external solution is required. A pulse-width modulation (PWM) output

from the microcontroller is used and the output voltage is smoothed with two RC low-pass filters. The amplifier then boosts the filter's output signal to maintain full functionality without overloading the low-pass filter. To develop the DAC, it is simulated in LTspice to verify that the output signal is smooth enough. Figure 5.15 shows the simulation model. The duty cycle of the simulated PWM signal is changed over time in order to adjust the frequency ramps that are used for the frequency control of the radar. The result generates a saw-tooth signal shown in figure 5.14 that the filter smooths a 7.8 kHz PWM correctly. Since the function is given for a saw-tooth signal, this is also validated for a triangle signal. Refer to Figure A.18 for the exact connections of the microcontroller and the implemented DAC.

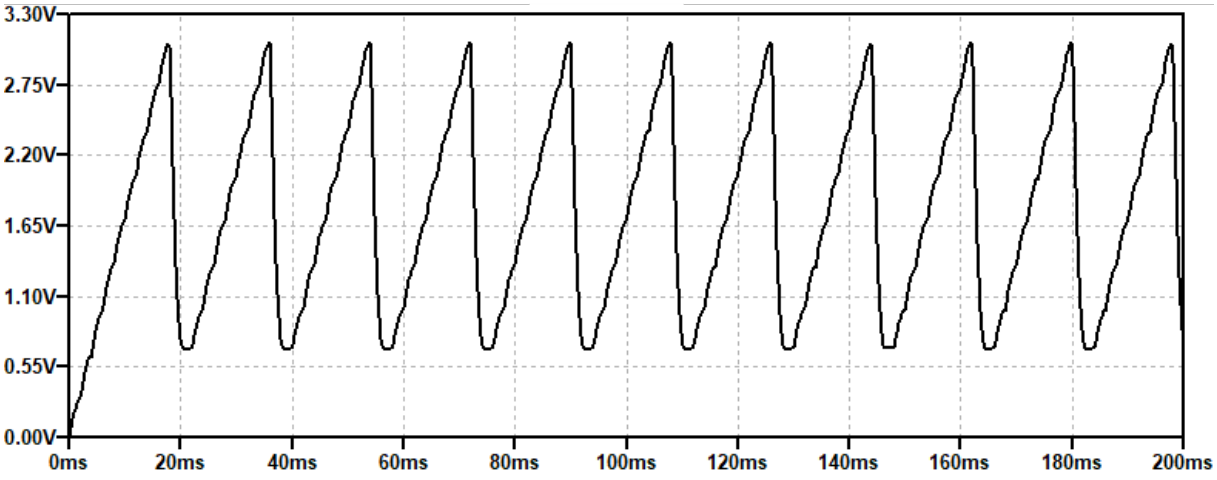

Figure 5.14: Triangle voltage output of the DAC in LTspice

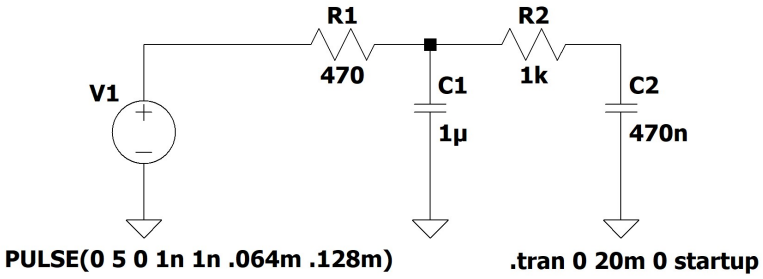

Figure 5.15: Simulation model of the DAC in LTspice

5.2.3 Typical automotive circuit

The sensor system will serve as a standard control unit in the automotive industry. To ensure realistic research, the system complies with automotive standards. At the plug connection, there are terminals for KL30, the permanent positive pole in the vehicle, KL31, the ground path in the vehicle, a wake-up pin, and a data bus connection. The research work employs an I2C bus instead of the CAN bus used in cars due to its complexity and licensing. Reverse polarity protection is also included within the circuit diagram. For more current-intensive circuits, a

MOSFET is utilized for this purpose in the automotive industry. Since no substantial currents flow through this control unit, a basic diode is employed. KL30's supply voltage is continuously measured by the microprocessor, as is customary in the automotive industry. A voltage divider is installed to measure a minimum of 24 V in order to prevent overloading the microcontroller input during a jump start. Additionally, measures are taken to comply with the quiescent current requirements of the automotive industry, which are typically 100 µA. To aid in this requirement, the microcontroller is able to switch the radar chip and its power supply, the 3.3 V linear voltage regulator. The 2.5 V reference voltage in the amplifier circuit can also be turned off by the microcontroller. Furthermore, the microcontroller can also turn off its own supply voltage however, it can only be reactivated by an external wake-up signal to exit sleep mode. The detailed schematic is shown in Figure A.18 for specific details.

5.3 PCB design

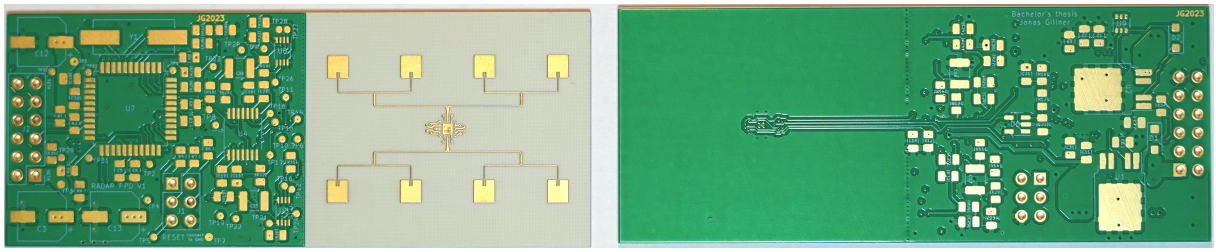

Figure 5.16: Front and rear side of the non-equipped PCB

A circuit is formed from all the components listed here, with the circuit diagram available in Figure A.18. The PCB implementation of the circuit should be as compact as possible, as there is limited space in the car to fit the control unit, and each circuit board piece comes with its own expenses. To enable space-saving track connections between individual components, the PCB is designed with 4 layers. The design adheres to the supplier's rules outlined in Section 5.1.2. A hybrid "sandwich" layer structure of the PCB is in place, with the high-frequency material RO4350B used only for the antenna structure. The substrate is made of the desired high-frequency material between the first and second, and the third and fourth layers, improving the connectivity of the PCB. The layer between the second and third layers is composed of standard FR4 to reduce costs, given that RO4350B is noticeably more expensive than FR4.

When placing components, it is ensured that the RF and LF parts of the circuit are kept separate to avoid interference. Refer to figure 5.16 for a clear visual of this, where the LF part is on the left and the RF antenna structure is on the right, which the solder mask intentionally does not cover, mimicking the simulated antenna. The antenna functions for both transmission and reception, while the chip is positioned between the two antennas equidistant. On the right side of the image, the rear side is visible. Specifically, the LF portion situated at the back and behind the LF part on the top side can be seen due to the rotation. The traces leading to the radar IC

are located underneath the RF portion on the back to ensure that they are not disrupted by the antenna structure and do not affect it. Additionally, multiple test points are integrated into the board which permits individual signals to be evaluated by the oscilloscope. All test points are located at the front for simplified testing. These test points are also utilized in the automotive industry for microcontroller flashing.

The production of the high-frequency PCB takes 15 working days, which along with delivery time, accounts for almost one-third of the processing time for this research work from order to delivery. According to the methodology, the PCB is ordered as a pure FR4 board in order to practice the assembly and operation of the circuit to partially complete the software.

Both the plain FR4 board and the hybrid high-frequency PCB are manually assembled by applying solder paste to the pads using a stencil, placing components, and heating the board with a reflow heating plate to complete the solder process. It is important to note that this process can only be performed on one side of the PCB to avoid the components on the lower side from falling off during the heating process. Therefore, when designing the PCB, it is taken care to plate the majority of components on the front side and place particularly small footprints on that side as well. To solder the back side, a stencil is used to apply solder paste. Once the components are placed, the back side is soldered using a hot air gun, which allows to heat the pads specifically and avoid overheating the board or causing components on the opposite side to fall off. Figures 5.17 and 5.18 depict the fully assembled PCB.

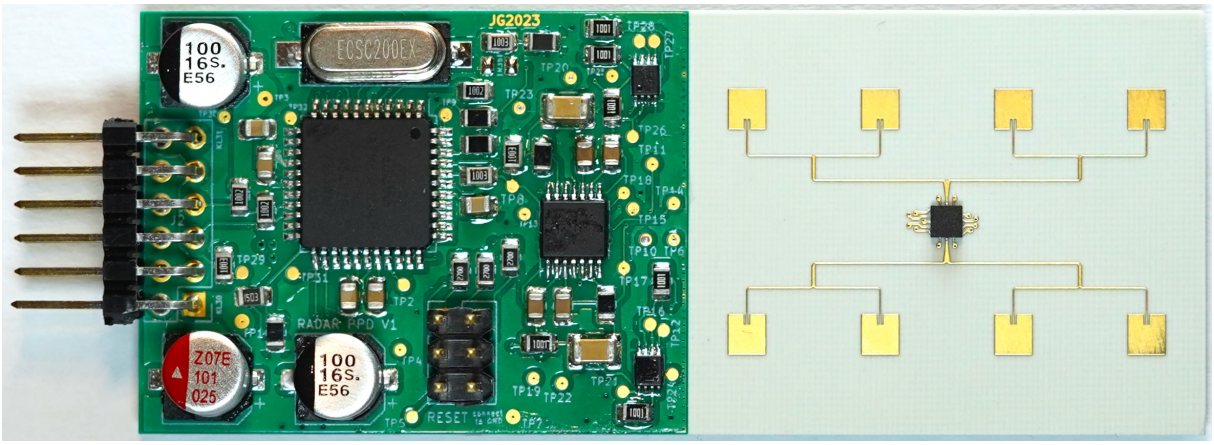

Figure 5.17: Front side of the assembled PCB

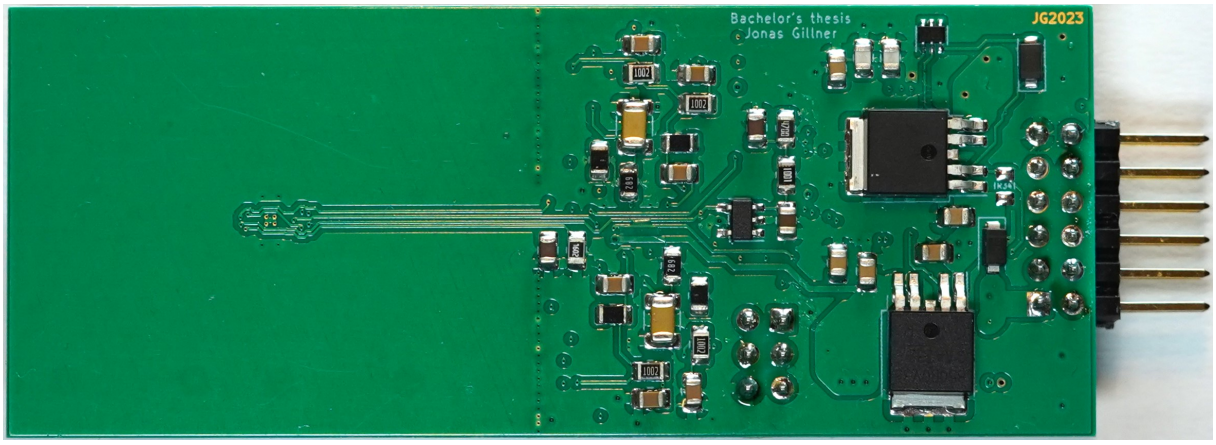

Figure 5.18: Back side of the assembled PCB

5.4 Software

The microcontroller software is divided into three main areas. The first is to control the radar frequency, followed by recording and processing radar output values. Finally, a main system operation is required to offer a user interface during development and transmit data via bus.

5.4.1 Control the radar frequency

To determine frequency, the microcontroller retrieves the current radar IC frequency and adjust as needed. The microcontroller can read the clock signal generated from pin 8 of the radar IC. This pin outputs the current radar frequency divided by 8192, resulting in a signal operational within the range of 2.9297 MHz and 2.9602 MHz, which is a frequency range the microcontroller can observe. Pin 41 of the Atmega1284P is linked to timer 1, and can be utilized as the external clock to read in the detected signal. This means that timer 1 increments by one with each cycle of the clocked signal. The measurement is taken over a specified duration and then extrapolated. Selecting a longer time period results in a higher frequency accuracy. In CW mode, frequency control is simple and straightforward. The process is implemented in lines 244 to 265 of source code A.3. The frequency input is checked to ensure it falls within the defined range. If not, the analog setting voltage at pin 14 of the radar IC is adjusted through the generation of a PWM at OCR0B pin 44 using timer 0 of the microcontroller. The DAC then converts the PWM to an analog voltage that depends on the duty cycle. If the measured frequency falls below the target 24 GHz frequency, the DAC is increased. Likewise, if it is above, the DAC voltage is decreased. When in FMCW mode, frequency control becomes more complex. Check lines 266 to 337 in the A.3 source code for more details. Not only must the frequency be monitored, but it must also be continually regulated to achieve the triangular modulation of the frequency as specified in 2.1. To achieve this, upper and lower limits are defined. Upper and lower limits are defined to regulate the frequency ramp movement. The duty cycle counts up and down

within these limits, generating an analog triangular signal at the DAC output. Due to the proximity of the signal frequency to 3 MHz, real-time frequency measurement with a 20 MHz clock frequency is unfeasible; instead, the edges are counted over time. Therefore, continuous control is not achievable. To compensate for temperature-induced drift, a modified method is employed. Every 100th rising ramp is halted at the midpoint of frequency measurement, and its edges are tallied. The technique yields sufficient accuracy for the anticipated measurements of the sensor system. If this value deviates upward or downward, the system recognizes that the ramp's boundary values must be raised or lowered. The technique yields sufficient accuracy for the anticipated measurements of the sensor system.

5.4.2 Data record and analysis

Recording and analyzing radar data is crucial for the development process. The radar IC generates analog voltage values that represent the I&Q-values of the beat frequency. These values are then amplified through the circuit in Section 5.2.1 to enable reading by the ADC microcontroller. Since each I&Q-value requires two amplifier stages, a total of four values must be recorded. The functions from lines 144 to 187 read and store these values in an array at the start of the measurement. The offset, around which these values oscillate, is initially obtained from the read values. The 2.5 V specified in the circuit is the offset for high gain, whereas the offset for low gain is unknown. To determine this, the raw values of the I&Q-value before the measurement starts are recorded, with the radar transmission switched off. Note that the capacitors in the amplifier circuit are pre-charged before recording initialization values. This permits offset subtraction in lines 339 to 353. To save on RAM, the values in the array are replaced and no other array is utilized. To analyze the data, the phase is calculated utilizing formula 2.15 in lines 354 to 358, which represent the I&Q-values. A separate array is utilized to store the phase in floating point format, with only one value saved for the low and high gain. Notably, it should be acknowledged that the atan2 function is not continuous, and it contains jumps. To account for these discrepancies, phase jumps are recognized and calculated using code lines 359 to 378. A basic frequency analysis is conducted to extract the respiratory frequency, obtained from research work [2], but it must be customized since the system now utilizes floating point numbers and detection values for the highest peaks in the frequency spectrum must be adjusted for this particular application. First, a mean value filter is applied to the phase between lines 379 and 391 as it is of interest. Next, the frequency spectrum of the data is blended between lines 406 and 426 and saved into an output array. Unlike the traditional Fourier transformation, binary cosine and sine functions are used for analysis, resulting in less calculation for the controller. The two rectangular functions are defined in lines 392 to 405. To extract the final breathing frequency, locate the highest peak where the magnitude surpasses a certain level within lines 427 to 452. Analyze only sections of the output array appropriate for measuring breathing frequency. Save the location of the peak. The system can then convert the position into bpm and check whether it falls within the defined breathing frequencies. If

the reading is within the defined parameters, the system will recognize that a baby has been detected. Note that the controller can only detect the breathing frequency in increments of two due to bpm extrapolation. Nevertheless, this is precise enough for the scope of the system's operation.

5.4.3 Main system operation

The primary function of the vehicle system is to transfer data to the mobile control unit when it detects the presence of a baby. However, since this feature is not available, as explained in 4, the output is redirected to an LCD display. The display shows the text "BREATHING: YES" if it detects breathing and "BREATHING: NO" if breathing is not detected. Furthermore, the eCall system can utilize detected breathing rate to inform the driver or emergency services regarding the child's potential age, like other systems discussed in 3.

6 System evaluation

The purpose of this chapter is to evaluate the individual functions of the developed sensor system. This includes testing, analyzing, and evaluating breath detection in the CW mode of the radar. Furthermore, the chapter evaluates the range measurement in the FMCW mode and characterizes the antenna's far field. Finally, the system undergoes evaluation with a real infant, representing the most significant measurement in this research.

6.1 CW breathing measurement

To assess and evaluate the detection of breathing rates in CW mode, measurements are performed on an individual with a height of 172 cm, aged 22 The individual under test is instructed to simulate various breathing rates or to stay out of the measured seat, allowing for an assessment of the system's capability to recognize different scenarios. During testing, the subject wears a heavy winter coat to showcase the advantages of the system outlined in the introduction. This results in the absence of visible breathing movements in the test subject.

6.1.1 Setup and performance of the breathing frequency measurement

The sensor system is affixed to a tripod tilted at a 45° angle and situated slightly above the head of the seated test individual, positioned approximately one meter away. The testing procedure involves initially taking a measurement without the test subject, followed by the subject entering the radar's field to simulate various breathing frequencies to assess the system's performance. Throughout these measurements, data is captured using a USB oscilloscope for subsequent evaluation. The oscilloscope data is then processed with MATLAB to confirm that the peak of the breathing frequency consistently maintains its position.

6.1.2 Results of the breathing frequency measurement

The initial measurement is void due to the absence of a test subject on the measured seat, as previously described. Consequently, Figure 6.1 exhibits no phase fluctuations, indicating that the sensor system registers no respiratory activity. The peak detected at a frequency of 0 Hz in this figure represents the DC peak.

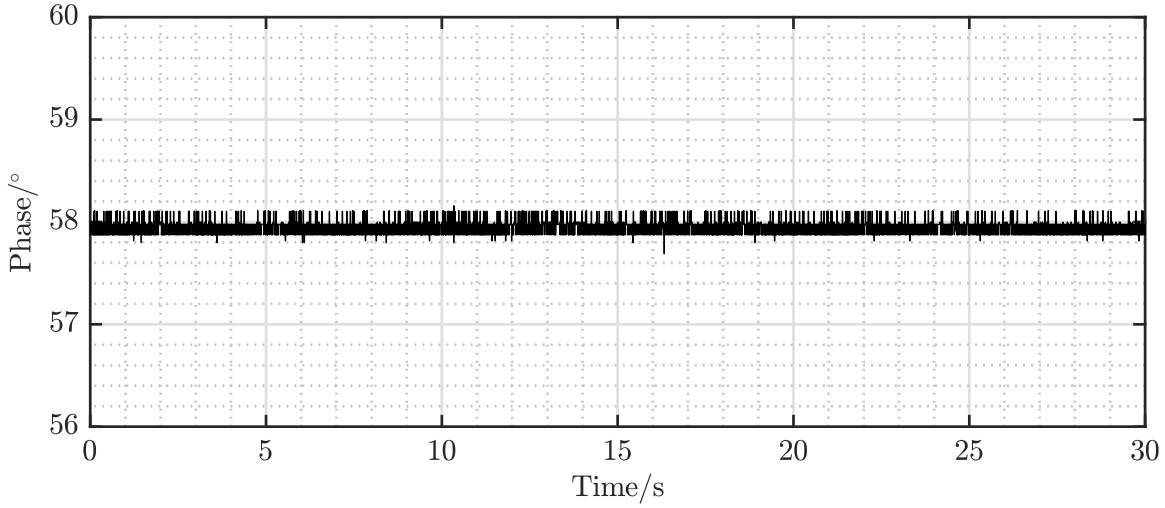

Figure 6.1: Phase of the test measurement with an empty seat

In the second showcase measurement, the test subject attempts to inhale every 3 seconds, and the resulting phase response is depicted in Figure 6.2. A noticeable oscillation is evident compared to the unoccupied seat showcase measurement and the simulation clearly depicts 10 oscillations. The microcontroller of the sensor system successfully detects and validates the observed breathing. In this case, the processing algorithm measures the breathing rate at 20 bpm.

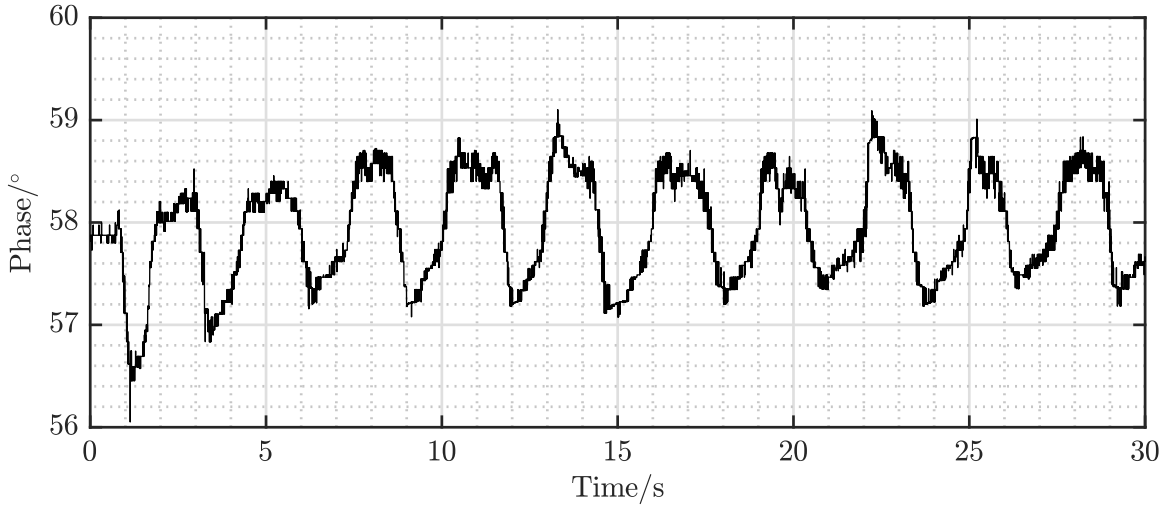

Figure 6.2: Phase of the test measurement with a defined breathing frequency

In the third measurement, the test subject engages in extremely shallow breathing without substantial chest movements or aiming for a specific breathing rate. Figure 6.3 illustrates that the amplitude of oscillation has significantly reduced compared to 6.2, making it challenging to discern the number of oscillations. However, the microcontroller is able to detect breathing at a frequency of 24 bpm and provide an indicator displayed on the LCD.

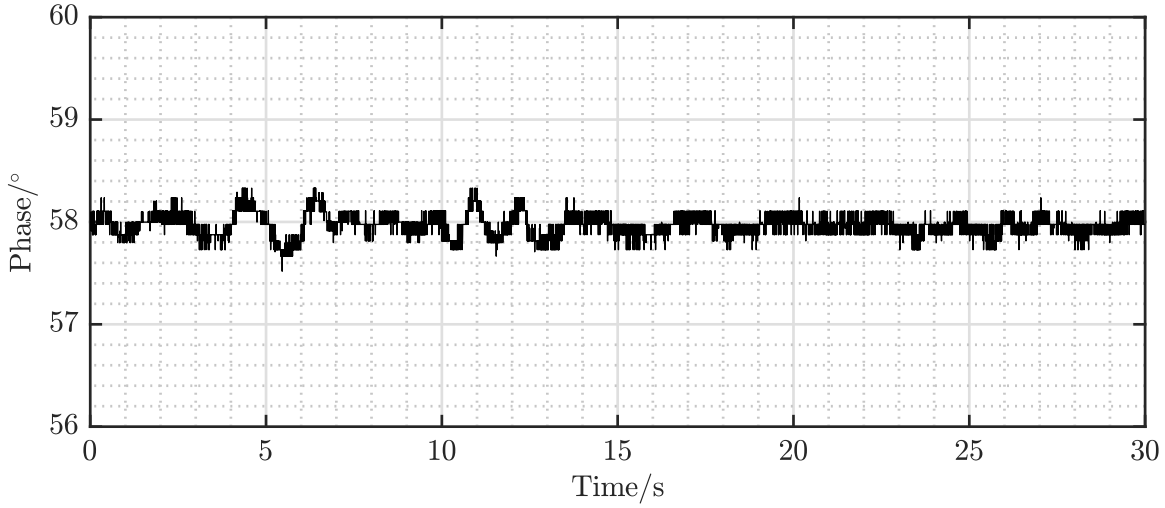

Figure 6.3: Phase of the measurement test with low amplitude breathing

6.1.3 Discussion of the results

Unoccupied seat: The sensor system accurately detects the absence of breathing during the unoccupied showcase measurements, as confirmed by the fast Fourier transform (FFT) applied to the phase in MATLAB. The plot is intentionally presented with a logarithmic Y-axis to illustrate the minuscule peaks. This suggests that the sensor system does not induce any false detections and, subsequently, does not trigger false alarms.

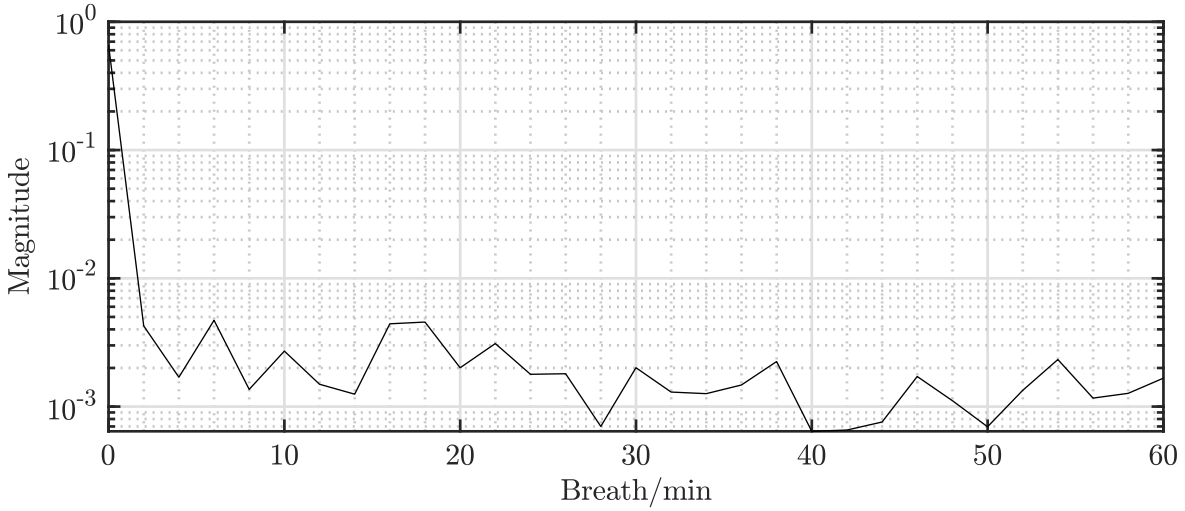

Figure 6.4: FFT analysis of the test measurement with an empty seat

Occupied seat with breathing subject: The microcontroller identifies 10 oscillations generated by test subjects during measurements as indicative of breathing. This is further validated by applying the FFT to the phase in MATLAB, as depicted in Figure 6.5, enabling precise determination of breathing frequency and preventing false detections by the sensor system.

This approach facilitates the assignment of a breathing rate to an age category and triggers alarms specifically for infants left behind.

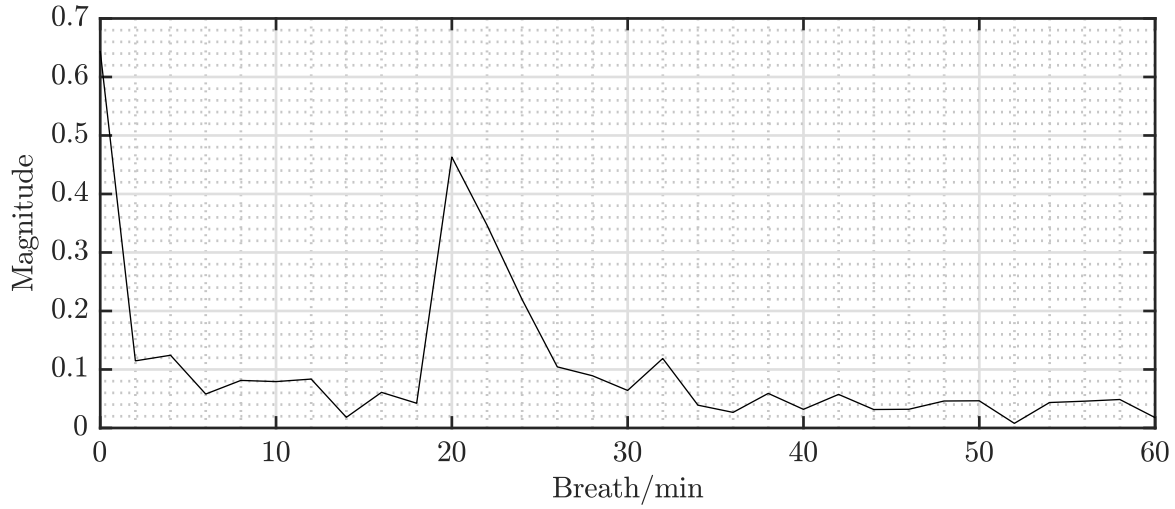

Figure 6.5: FFT analysis of the test measurement with a defined breathing frequency

Occupied seat with shallow breathing: The microcontroller identifies breathing despite slight oscillations during shallow breathing. A direct FFT comparison in Figure 6.6 confirms accurate detection, with the highest peak at 24 bpm, confirming the sensor system's reliability. The device's high accuracy allows for the detection of even the subtlest chest movements, which is crucial given that a baby's breathing movement is considerably less pronounced than that of an adult. It can be safely assumed that detecting a baby's breathing with the device would pose no challenges.

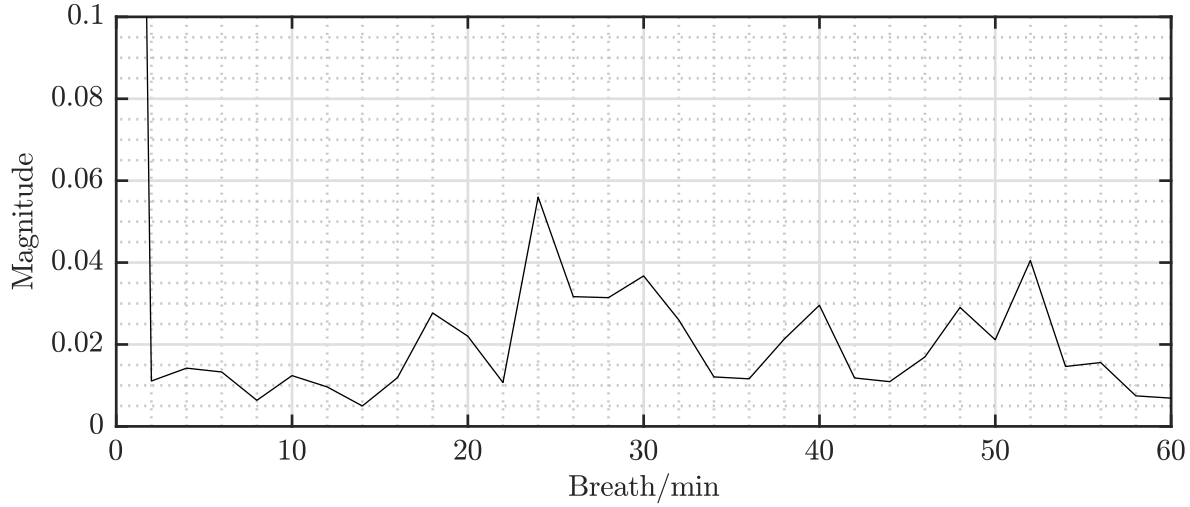

Figure 6.6: FFT analysis of the measurement test with low amplitude breathing

6.2 FMCW distance measurement

In this section, distance measurement in FMCW mode will be evaluated. For this purpose, the distance to an object is to be measured and extracted from the sensor data read in.

6.2.1 Setup of the FMCW test

An initial measurement is conducted to establish baseline values. The system is positioned in an open area to eliminate any objects within the antenna lobe's range. During distance measurements, the sensor is mounted on a tripod and precisely aligned to ensure the antenna lobe hits the object vertically. The I&Q-of the signal are recorded at different distances between the antenna and the object. The data from both measurements is captured using a USB oscilloscope for signal analysis and distance extraction.

6.2.2 Results of the FMCW setup

The preliminary measurement results indicate a distinct oscillation of the I&Q-values with a steady frequency of 106 Hz, as displayed in Figure 6.7. The black curve represents the I-value from the first amplifier stage, while the gray curve corresponds to the Q-value. This observed pattern remains consistent in all subsequent figures.

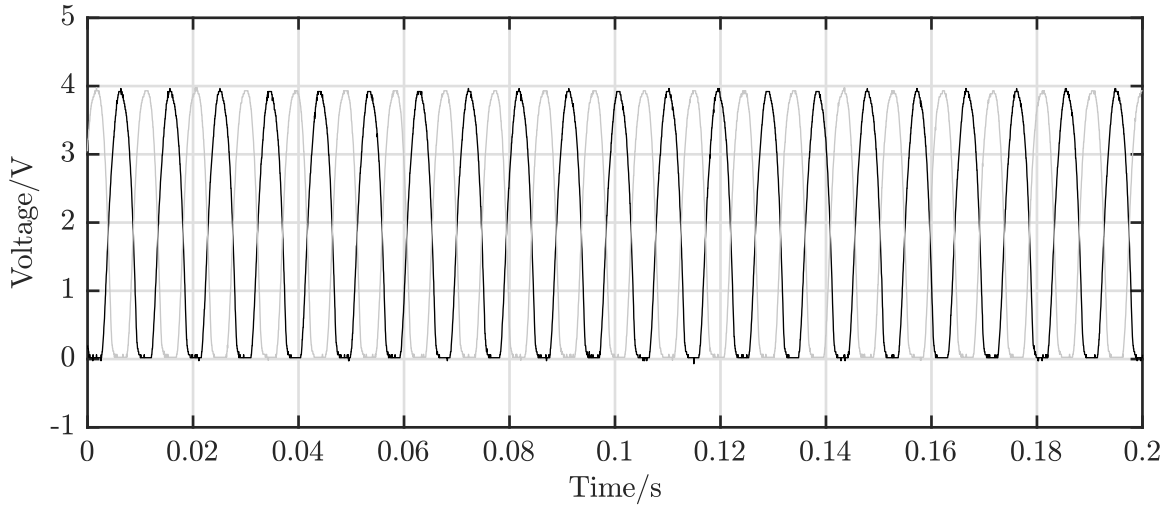

Figure 6.7: Illustration of the I&Q-values in FMCW mode for empty measurement

Measurements with a reflecting object within the radar range are recorded at three distinct distances. Throughout these measurements, the distances vary within one wavelength. The results are presented in Figures 6.8, 6.9, and 6.10. Figure 6.8 depicts I&Q levels that are nearly identical. The frequency of the recorded signals remains at 106 Hz. In Figure 6.9, the I-signal

remains unchanged, while the Q-signal height is reduced for this distance, with a modulated signal present. In Figure 6.10, the opposite is observed, where the Q-value is in its normal form, and the I-value is superimposed. The modulation on the signal has a noticeable higher amplitude than the dip before. Nevertheless, both superpositions have a lower amplitude than the initial signal. It can also be observed that the modeling is the same in each cycle and that there is no modulation over several cycles.

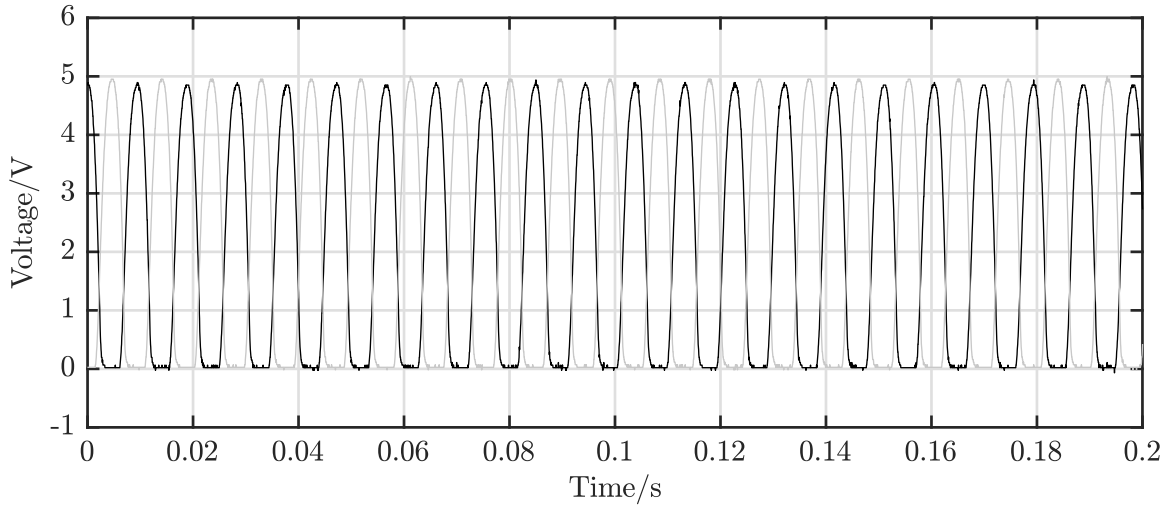

Figure 6.8: Illustration of the I&Q-values in FMCW mode for measurement of distance 1

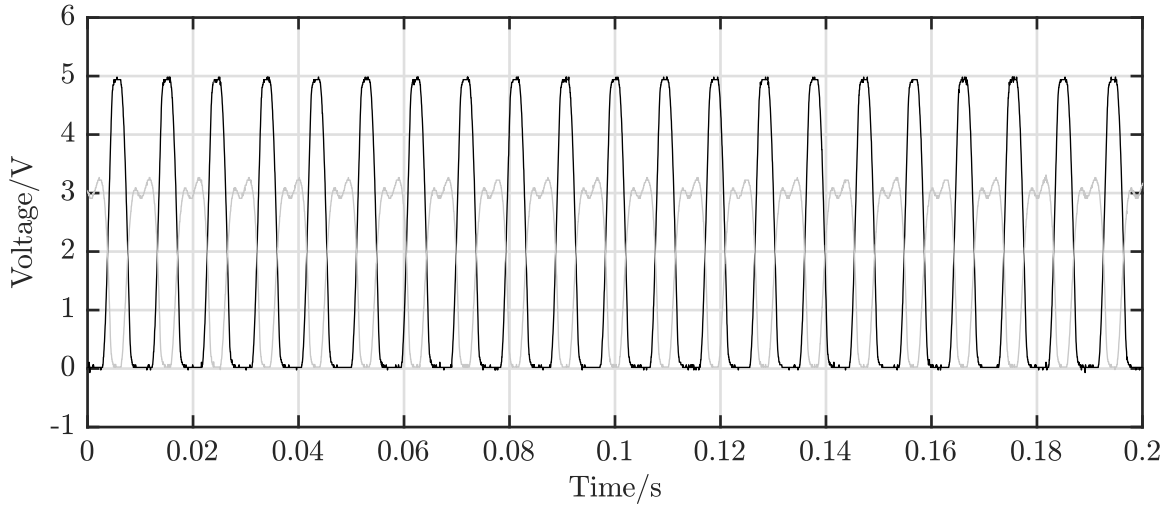

Figure 6.9: Illustration of the I&Q-values in FMCW mode for measurement of distance 2

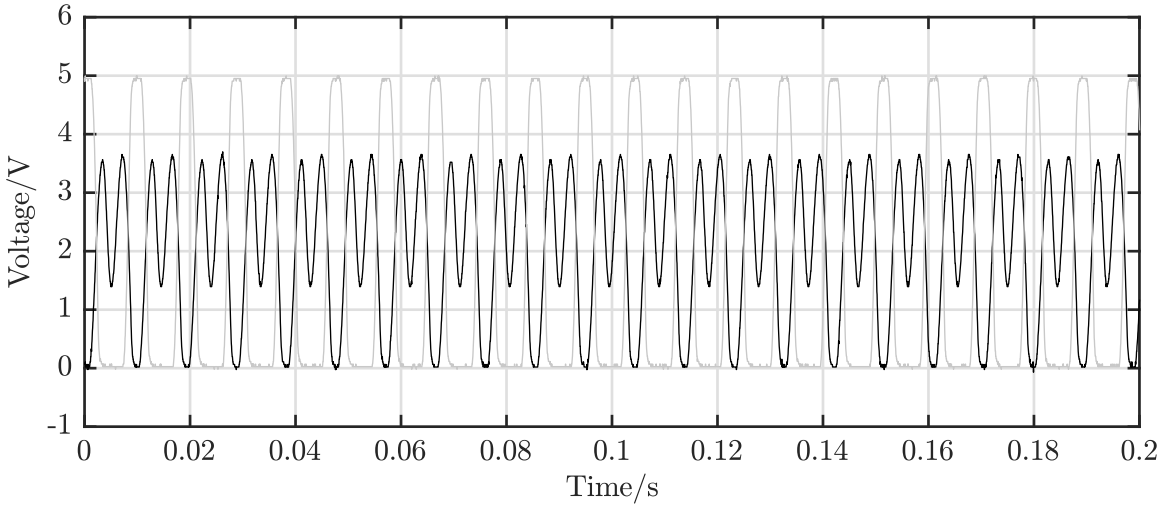

Figure 6.10: Illustration of the I&Q-values in FMCW mode for measurement of distance 3

6.2.3 Interpretation of the FMCW measurements

In the results of the FMCW measurement, a distinct fundamental frequency of 106 Hz is evident. It is assumed that this is due to over-coupling between the two antennas. If another distance is modeled into the signal, its amplitude is to low to overwrite the fundamental wave. This also indicates that the fundamental is due to the distance between the two antennas because this is the shortest distance, which leads to the highest amplitude. The fact that the modulation starts anew in each cycle is due to the FMCW operating mode. Triangle modulation causes two moments per period where the transmit and receive frequencies match. For this moment, the beat frequency is 0 Hz. Regarding to this the signal of the beat frequency starts from beginning again every time.

Coincidentally, the frequency of the ramps used for frequency modulation also matches the measured frequency of the fundamental signal. To find a relationship between this, the Q-signal is recorded together with the analog voltage for the frequency modulation, as shown in Figure 6.11.

Both signals have the same frequency, which is confirmed by adjusting the ramp frequency. The base frequency shows an identical change, aligning with the FMCW principle from Section 2.1. As this fundamental frequency is constant, it results from over-coupling between both antennas and corresponds to their distance. Applying formula 2.3 shows a distance of 0.6 m. The measured distance between both antennas is inaccurate. To validate the measurement, a metal plate is inserted between the antennas to reduce over-coupling between the transmitting and receiving antenna. A noticeable decrease in amplitude confirms over-coupling as the cause of the error. To solve the false measured distance between both antennas, additional research is done.

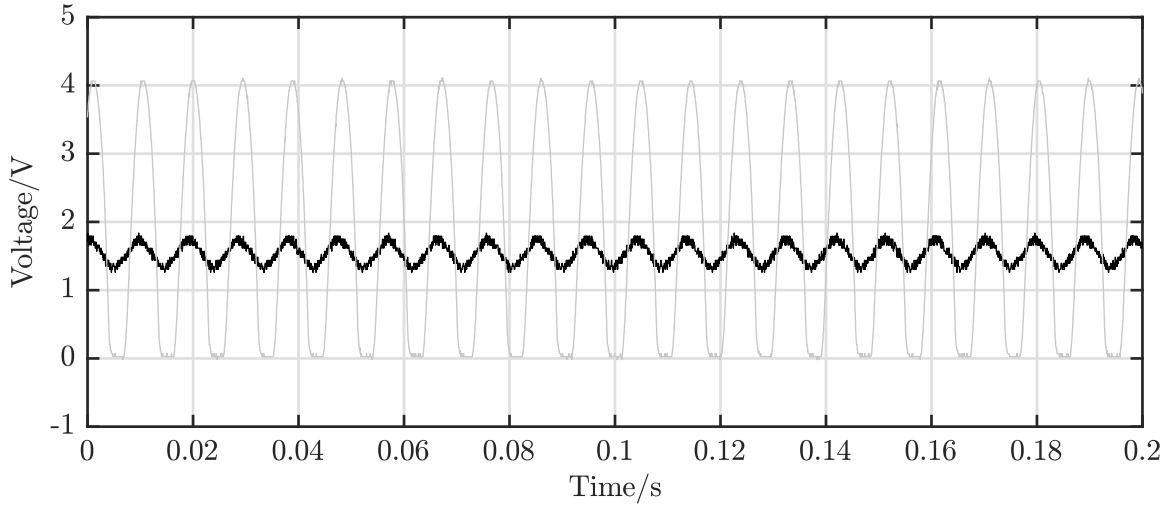

Figure 6.11: Illustration of the Q-value and the frequency modulation voltage in FMCW

$$R_{\text{res}} = \frac{c}{2 \cdot B} \tag{6.1}$$

Formula 6.1 is found in [6] to calculate the range resolution of the sensor system. The calculated range resolution is 0.6 m. With this result the wrong distance between both antennas can be explained. The calculated distance is the minimum recognizable distance causing the range resolution of 0.6 m. This also gives an reason for the superimposed signal. These are only harmonics of the fundamental wave, because the doubled frequency of the beat frequency signal leads to a doubled distance. The doubled distance is the next detectable range.

6.2.4 Discussion of the problems in distance measuring

The relationship found between the two antennas in the fundamental wave poses a problem for distance measurement. Since the further distances with low amplitude are of interest for the application, the fundamental wave must be removed from the signal. This should not be a problem with a suitable filter circuit at the amplifier stages. However, since low frequencies are relevant in this application to detect breathing, it is not possible to adapt the amplifier circuit by redesigning it to filter out low frequencies. This leaves the solution of software filtering. At first, the signal appears to be unknown. In detail, there is the relationship between the ramp frequency and the fundamental signal. With this knowledge there is a way to extract the measured signal from the fundamental signal which is caused the over-coupling of the antennas. After this the remaining signal includes the distances. This signal extraction can be done by the microcontroller. During the initial measurement the microcontroller can record the I&Q-values together with the state of the analog voltage ramp. For this, it is not necessary that the controller reads the voltage of the ramp. It is enough to record the internal variable state for this. During the distance measurement the controller can subtract the fundamental wave,

recorded in the initial measurement, depending on the state of the ramp. Nevertheless, due to the following problem with the resolution and the short time period for this research work, an implementation is decided upon. The radar chip defines the bandwidth of the system. In this case it is defined as 250 MHz. Unfortunately, this also results in a rank resolution of 0.6 m, which is unusable for the application. However, it has already been proven that the breathing frequency can be detected with the sensor system. A distance measurement in FMCW mode would therefore only be a supplement to detect if there is anything on the seat at all. However, this is not necessary to ensure the functionality of the system.

6.3 Antenna characterization

The analysis of the developed sensor system indicates the antenna's accuracy. As stated in Chapter 4, the antenna is evaluated for its intended use and compared with the simulated results obtained during the design phase. However, equipment and time constraints prohibit a thorough analysis of the reflection and transmission, prohibiting an external measurement. As a result, characterization is focused solely on the beam and its beam angle.

6.3.1 Experimental setup and performance of the characterization

For the intended purpose, a high-frequency reflector is used consisting of three identical right-angled triangles made of copper or other applicable metals. These triangles are interconnected in a way that creates a common center with adjacent edges connected to the edges of the other triangles. The reflector is shown in figure 6.12. As a result, incoming waves are uniformly reflected at the same angle of incidence. To determine the radiation angle of the antenna, measure the reflector's distance using FMCW with 0° radiation angle towards the target. This distance serves as the reference point, and the antenna is then rotated horizontally and vertically. Once the reflector is no longer visible in the ranging, the end of the beam can be identified. The peak of the range should weaken towards the edge, allowing for attenuation to be specified in dB relative to the angle. To conduct the measurement, mount the antenna on a rotating plate with angular dimensions to easily take readings at specific angles. Unfortunately, this method cannot be used because the distance measurement is not included, as described in Section 6.2.4.

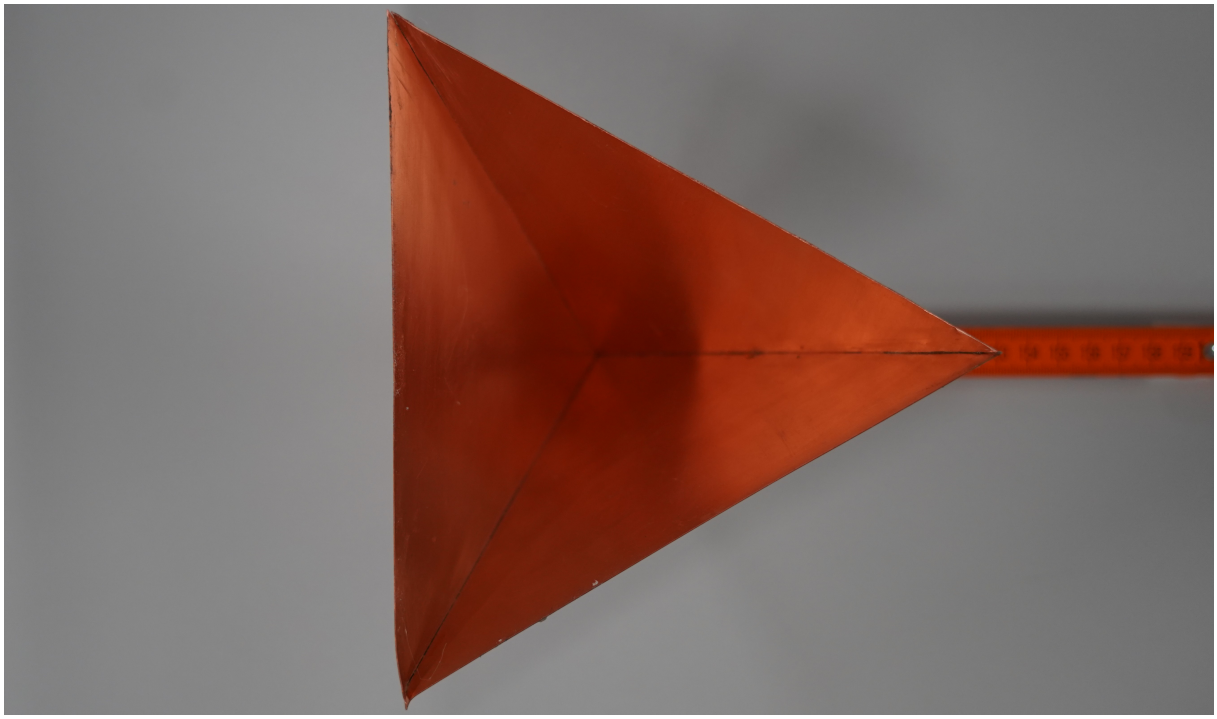

Figure 6.12: Self-built RF reflector for antenna characterization

Instead, characterization can be carried out in CW mode by placing the reflector in front of the antenna with a radiation angle of 0° and setting the distance at 1 m for this measurement. The antenna is mounted on a turntable, which is placed on a trolley to generate minimal oscillation in the forward and backward direction. The setup is shown in figure 6.13. The Doppler effect causes deflection in the I&Q-values recorded during oscilloscope measurement. Formula 2.14 and recorded I&Q-values are used to calculate the amplitude of beat frequency fB. Next, the turntable is rotated in two directions, and intermediate values are recorded at the edge positions. The angles of ±5°, ±10°, and ±15° are recorded horizontally, while ±80°, ±90°, and ±100° are recorded vertically to find the edge positions of the lobe.

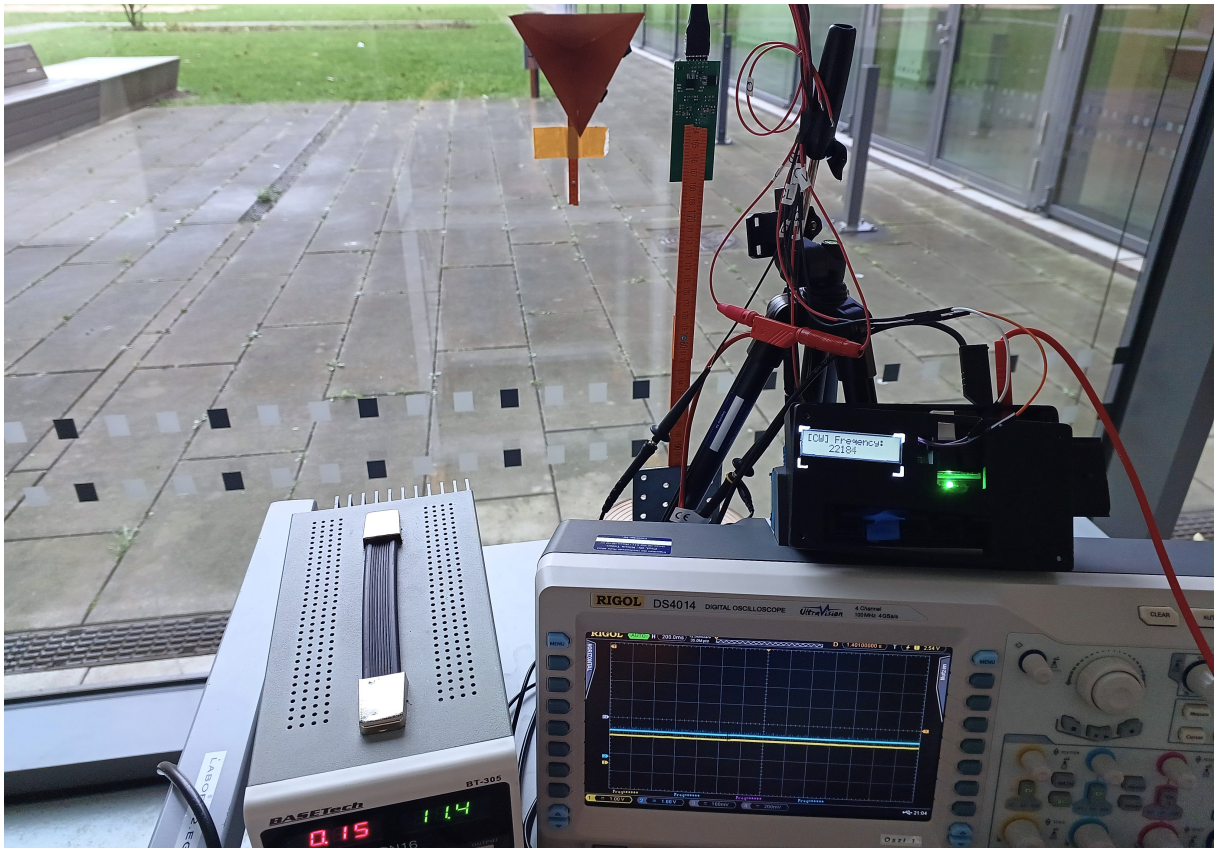

Figure 6.13: Measurement setup of the antenna characterization

6.3.2 Results of the characterization

Figures A.4 and A.11 depict this calculation for zero measurement in the horizontal and vertical directions respectively over time. These edge positions are the result of the lower amplitude until deflection is nearly non-existent. as shown in Figures A.5-A.10 for the horizontal and A.12-A.17 for the vertical. Based on the measurements, the deflection angle can be narrowed down in both horizontal and vertical directions. The range is approximately -15°/-10° to 10°/15° horizontally and -110°/-100° to 90°/100° vertically.

Place here the polar pattern diagram

6.3.3 Interpretation and discussion of the characterization

A comparison of the measured values with the simulated values demonstrates a fairly accurate correspondence. In the simulation, the radiation angle has a defined limit value of 3 dB at 16.7° in the horizontal direction. Figure A.9 displays a negligible amplitude around 15° during characterization. Additionally, the polar pattern plot in Figure 5.4 illustrates a noteworthy decrease in lobe up to 16.7°. Figure A.7 demonstrates that the amplitude at 10° is markedly

lower than that at 0° in Figure A.4, further corroborating the simulation results. A similar pattern is observed in the vertical characterization. The simulation defines the limit value of the radiation angle as 3 dB at 116.2°. Measurements define angles up to 100° and 110°. The simulated polar plot also displays the asynchrony, further validating the simulation results. The ground plate's position is responsible for the asynchrony.

One crucial aspect to note is the lack of a professional characterization method. Nevertheless, the comparison results confirm the quality of both the used characterization method and the designed antenna. This underscores the necessity of using this methodology to save time in this short project. The alternative method yielded results with sufficient accuracy and satisfactory outcomes. The antenna operates similarly to the simulation, allowing for the behavior of the manufactured antenna to be compared to that of the simulation.

6.4 Detection of the breathing from an infant

To conclude the study, the developed system is tested with a real child to confirm the function of the developed prototype.

6.4.1 Description and execution of the final test case

The child is approximately 2 years and 5 months old and 1 meter tall. The measurement is carried out while the child is asleep in a kindergarten. No photo is provided to protect the privacy of the child, but a modified test setup is depicted in 6.14, showing the infant in a child seat on the car seat. The sensor system, utilizing radar technology, is located in the headliner and emits signals from above, enabling detection of the child. Alternatively, it can be installed in the seat backrest. The child dummy depicted in the illustration is small, and therefore positioned rear-facing in the car seat. However, the radar signal can penetrate the child seat, rendering installation direction immaterial. Detection can be accomplished in both seat positions.

Figure 6.14: Exemplary setup of the measurement in a car

In the actual measurement setup, the child lies on its stomach on a mattress in a dark room. The antenna is positioned beside the sleeping child at about 1 meter away. This ensures that the sickle-shaped beam of the antenna is not spread lengthwise from top to bottom over the child, but rather crosswise. Although this is not the usual detection direction since it covers less of the child's body, it is necessary in this case. However, this is not an issue as it increases the complexity of measuring the test system. If the sensor can detect breathing despite the set conditions, it highlights the robustness and quality of the developed system.

As described in Section 5.4.2, the measurement principle involves recording data for 30 seconds using the battery-operated sensor system to ensure mobility. Following data collection, the microcontroller calculates and displays the result on the LCD. Additionally, I&Q-values are acquired using the USB oscilloscope and documented to allow simulation and verification of the chip calculations in MATLAB. The child measurement is repeated multiple times with the specified setup to ensure it is reproducible.

6.4.2 Results of the final measurement

Figure 6.15 presents the I&Q-values captured by the oscilloscope after the first amplifier stage, showing a noticeable slight oscillation in both signals.

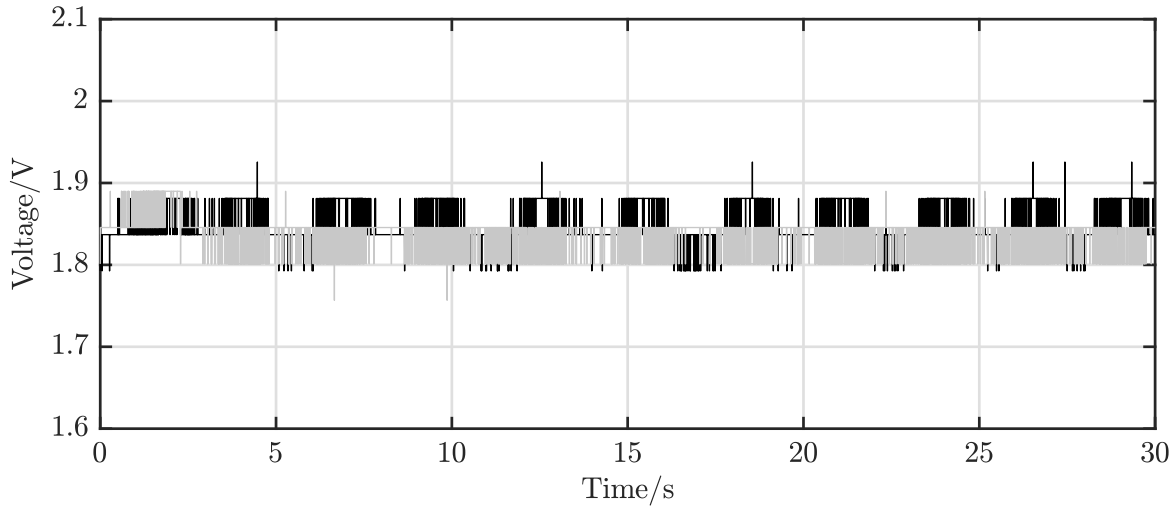

Figure 6.15: I&Q-values of the measurement with a child

These signals are then processed by the system's microcontroller. The signal processing algorithm, as demonstrated in Figure 6.16, identifies the most significant peak at a rate of 22 bpm.

Figure 6.16: Result the measurement with a child on the sensor system

This peak is interpreted by the sensor system as indicative of an infant's respiration, a conclusion supported by the visualization in Figure 6.17.

Figure 6.17: Interpretation of the measurement with a child on the sensor system

Throughout the measurements, the child's breathing remains consistent, resulting in uniform results. However, there is a deviation in the final measurement signal, as depicted in Figure 6.18. This deviation is attributed to the child's movement during the measurement, yet the system successfully continues to detect the infant's breathing despite this interference.

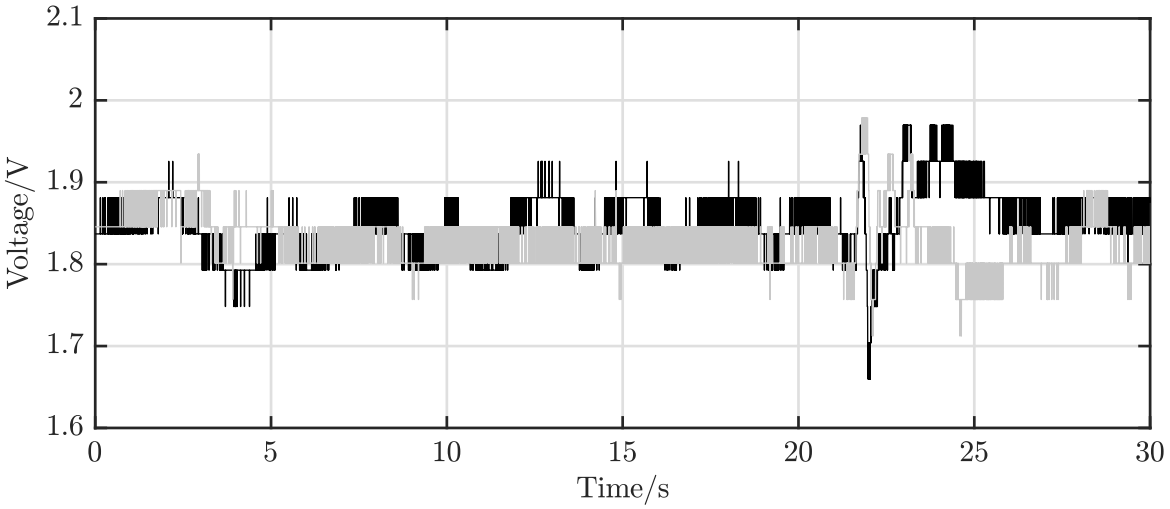

Figure 6.18: Disturbed I&Q-values of the measurement due to a moving baby

6.4.3 Analysis and interpretation of the measurement

To compare the signal processing of the microcontroller with a real FFT, the recorded data from the oscilloscope is analyzed in MATLAB. The formula 2.15 can be used to compute the phase of the sinusoidal beat frequency from the recorded values. The phase is presented in figure 6.19.

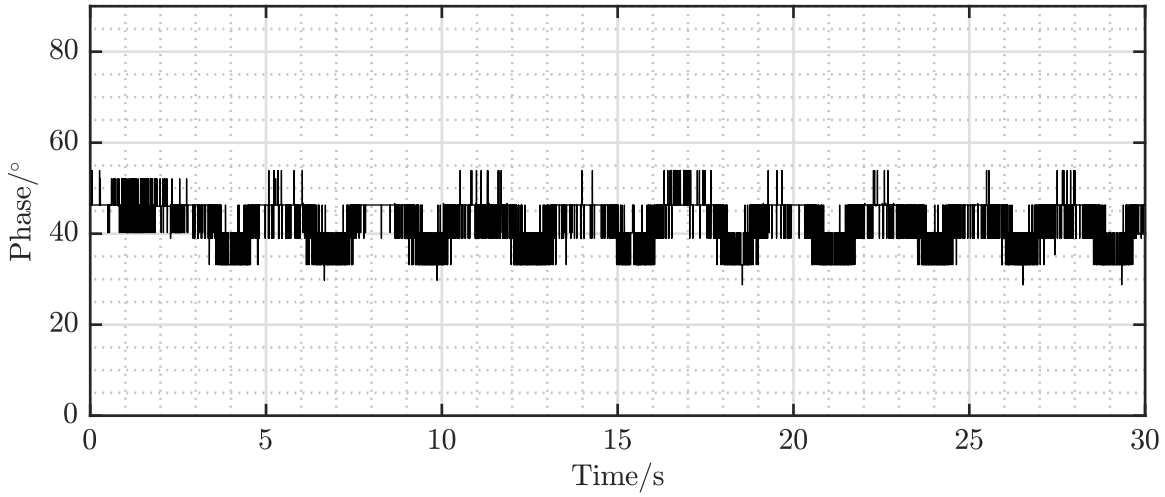

Figure 6.19: Phase of the measurement with a child

The respiration frequency for the operation is determined by extracting it from the phase signal. This analysis utilizes an FFT, with the resulting data displayed in 6.20.

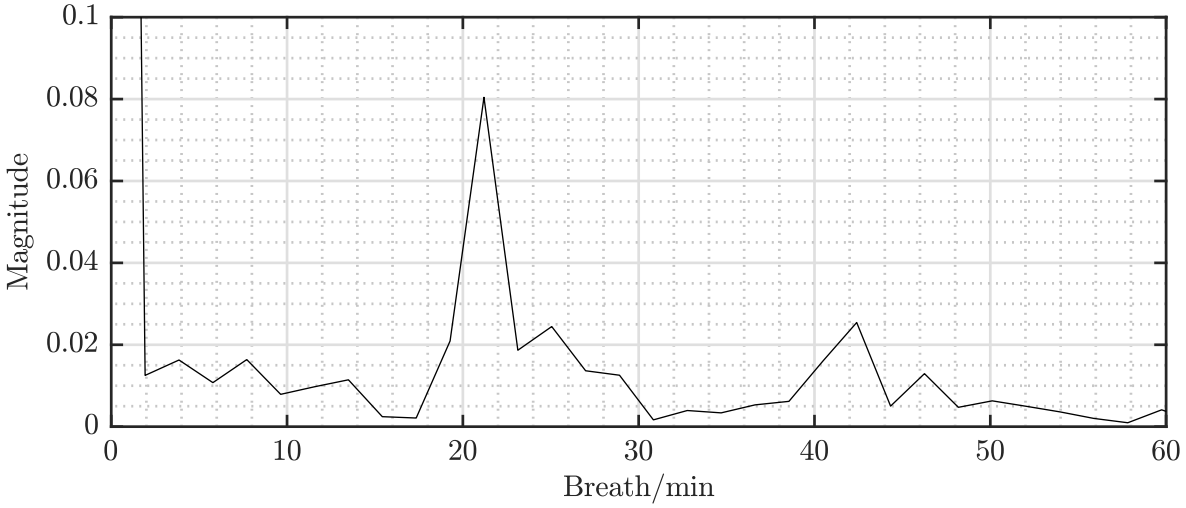

Figure 6.20: FFT of the measurement with a child

The highest peak, disregarding the DC offset, is located between 21 to 22 bpm.

This peak closely matches the extracted breathing frequency on the sensor system. The algorithm on the microcontroller is only capable of determining the breathing frequency per minute in steps of two, as described in Section 5.4.2. This means that both results match almost exactly. However, for a more comprehensive assessment, the frequency analysis tool that evaluates the microcontroller is also utilized in MATLAB. The oscilloscope signal is sampled at a 10 Hz rate in MATLAB. Then, every 10th value is saved into an array for ADC conversion. To calculate the ADC value, the measured voltage is multiplied by $\frac{1023}{5}$. With 10-bit resolution ranging from 0 to 1023, the ADC of the microcontroller compares the voltage to 5 V and displays it. The MATLAB algorithm generates a breath detection of 22 bpm, demonstrated in Figure 6.21.

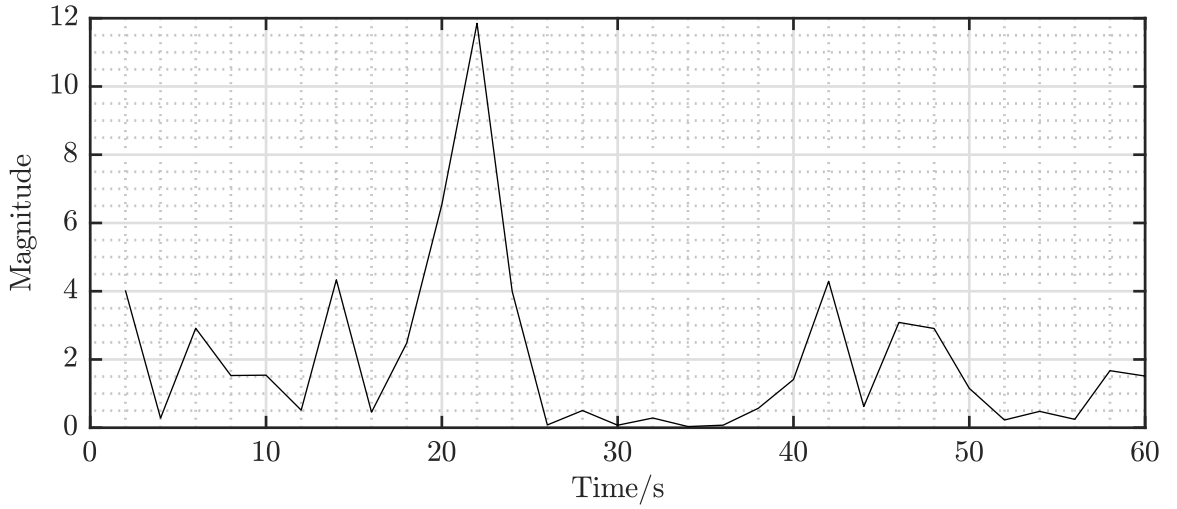

Figure 6.21: Frequency analysis of the measurement with a child from the microcontroller

6.4.4 Assessment of the final measurement

Finally, the results confirm the system's functionality. The system detected a breathing frequency, despite the weak oscillation caused by the child's small chest. The recorded breathing frequency aligns with the Euro NCAP protocol [3] for the infant's age, which is important for verifying the procedure and results of this study.

7 Conclusion

Based on the qualitative findings of this research, it is initially apparent that the developed sensor system is capable of accurately identifying infants. This indicates that the sensor system development methodology is appropriate and has been effectively implemented. Despite encountering certain impediments, such as a considerably long delivery period, the system was developed at a pace that allowed for thorough analysis and evaluation. The software utilized an existing signal processing algorithm, based on research work [2], in which the author contributed, to achieve its goals. The analysis and evaluation yielded qualitative results that corroborated the theory and previously conducted simulations. It can be concluded that the radar is highly effective in measuring respiration in CW mode, as the system can detect with remarkable accuracy. The slight rise and fall of a baby's chest during breathing generates a single oscillation large enough to extract the frequency of breathing. This indicates that the antenna, signal processing hardware, and software all possess excellent technical implementation and are well-suited for this automotive application. Omitting the FMCW mode does not pose any problems whatsoever. In fact, the system's functionality remains unaffected. On one hand, the board experiences less converted power due to the absence of continuous charging and discharging of the low-pass filter in the DAC. On the other hand, the software becomes simpler and shorter, leading to cost savings on components and controller RAM due to reduced signal processing. The objective of low-cost aspect is incorporated in all aspects of this work, resulting in attaining the goal.

8 Summary and outlook

An innovative automotive safety system was developed and presented in this thesis. This system can prevent child deaths if left behind in vehicles. Even if the sensor system developed in the research is never installed as a mass product in vehicles worldwide, it encourages the further development and installation of similar systems in all vehicles.

The low-cost sensor system developed is radar-based and was constructed on a self-designed PCB, which has been put into operation. The system contains a radar chip that operates in the K-band and can reliably detect the breathing of a small child in a qualitative manner. The system's powerful microcontroller processes raw measurement data and calculates the exact breathing rate of the child. Based on this information, the system accurately assesses whether a small child has been detected in the car by monitoring their breathing. If these conditions are met, the data is transmitted via a data bus to trigger immediate preventive measures. Extensive testing of the system was conducted during its development to ensure its long-term and reliable operation in a variety of scenarios. The system was intentionally designed to prevent fault detection. Despite this, it can reliably detect the slightest breath movements of an infant without any issues.

In summary, the radar-based sensor system developed by the scientific team effectively detects the presence of a small child and distinguishes it from inanimate objects on the passenger seat of a vehicle. It fulfills the primary objective of the study.

To improve this system in further works, the described FMCW problem should be fixed with the explained signal processing. In deeper subsequent research, a system can be devised by utilizing a phase array antenna. This thesis already explains the benefits of this type of antenna. A system with a phase array antenna will permit the monitoring of an entire vehicle by moving the antenna lobe. A phase-shifter is utilized for this propose. It is necessary to choose a frequency range that enables distance measurement with a more accurate resolution to accurately detect different locations in the car during the measurement. Another idea would be to explore potential integration of this system with other control units already present in the vehicle, as previously outlined in this paper. This approach can significantly reduce both the costs and space required for installation, both of which are critical considerations in modern vehicle development.

References

[1] Nsc Injury Facts. *Hot Car Deaths*. Motor Vehicle Safety Issuses. 2023. URL: https://injuryfacts.nsc.org/motor-vehicle/motor-vehicle-safety-issues/hotcars/.

[2] Leila Sharara et al. "An Intelligent Sensor-Based Back Seat Monitoring System for Preventing Pediatric Vehicular Heatstroke". In: *(in progress)* (2023).

[3] European New Car Assessment Programme. *Test and Assessment Protocol - Child Presence Detection v1.1*. Tech. rep. Euro NCAP, Jan. 2023.

[4] Albrecht K. Ludloff. *Praxiswissen Radar und Radarsignalverarbeitung*. Vieweg+Teubner Verlag, 2002. ISBN: 9783322995551. DOI: 10.1007/978-3-322-99555-1.

[5] S. Shamekhi K. Nordin. "24 GHz Patch Antenna Array Design for RADAR". MA thesis. Lund University, 2016.

[6] Mike Roberts. "24GHz FMCW Radar, Basic Theory and Real-World Measurements". In: (). URL: https://www.armms.org/media/uploads/mike-roberts---armms-nov-2019.pdf.

[7] Yeonghwan Ju, Youngseok Jin, and Jonghun Lee. "Design and implementation of a 24 GHz FMCW radar system for automotive applications". In: *2014 International Radar Conference*. 2014, pp. 1–4. DOI: 10.1109/RADAR.2014.7060385.

[8] Thomas H. Lee. *Planar Microwave Engineering. A Practical Guide to Theory, Measurement, and Circuits*. Cambridge University Press, Oct. 2004, p. 880. ISBN: 9780521835268. DOI: 10.1017/cbo9780511812941.

[9] Klaus W. Kark. *Antennen und Strahlungsfelder Elektromagnetische Wellen auf Leitungen, im Freiraum und ihre Abstrahlung. Elektromagnetische Wellen auf Leitungen, im Freiraum und ihre Abstrahlung*. Springer Vieweg, Feb. 2016, p. 572. ISBN: 9783658139643. DOI: 10.1007/978-3-658-13965-0.

[10] Ferdous Suliman and Ayhan Yazgan. "24 GHz Patch Antenna Array Design with Reduced Side Lobe Level for Automotive Radar System". In: *2020 28th Signal Processing and Communications Applications Conference (SIU)*. IEEE, Oct. 2020. DOI: 10.1109/siu49456.2020.9302104.

[11] Rick Hartley. "RF / Microwave PC Board Design and Layout". In.

[12] Kerstin Siebert. "Lecture - Hochfrequenztechnik und Elektromagnetische Verträglichkeit - 4 Leitungen". Apr. 2022.

[13] Talitha Strickler. "Zehn Jahre erhöhte Verkehrssicherheit durch Bosch eCall". In: *Bosch PI 11499 SO St* (June 2022).

[14] European New Car Assessment Programme. *eCall Additional Data Concept Triggering Incident*. Tech. rep. Euro NCAP, June 2022.

[15] marquardt. “Saving Children’s Lives With Artificial Intelligence”. In: *Press Release* (July 2023).

[16] continental. “Zugangslösung von Continental erkennt Kinder imFahrzeug und wird zum Lebensretter”. In: *Press Release* (Apr. 2023).

[17] A. Caddemi and E. Cardillo. “Automotive Anti-Abandon Systems: a Millimeter-Wave Radar Sensor for the Detection of Child Presence”. In: *2019 14th International Conference on Advanced Technologies, Systems and Services in Telecommunications (TELSIKS)*. IEEE, Oct. 2019. DOI: 10.1109/telsiks46999.2019.9002193.

[18] Andreas R. Diewald et al. “RF-based child occupation detection in the vehicle interior”. In: *2016 17th International Radar Symposium (IRS)*. IEEE, May 2016. DOI: 10.1109/irs.2016.7497352.

[19] Xiaolu Zeng et al. “WiCPD: Wireless Child Presence Detection System for Smart Cars”. In: *IEEE Internet of Things Journal* 9.24 (Dec. 2022), pp. 24866–24881. ISSN: 2372-2541. DOI: 10.1109/jiot.2022.3194873.

[20] *BGT24LTR11N16 - Silicon Germanium 24 GHz Radar Transceiver MMIC*. 1.3. Infineon Technologies AG. May 2018.

[21] *IEEE Standard Letter Designations for Radar-Frequency Bands*. IEEE Standards Board, Mar. 1984. DOI: 10.1109/IEEESTD.1984.81588.

[22] *BGT24LTR11N16 - DEMO SENSE2GOL PULSE*. 2.2. Infineon Technologies AG. Nov. 2023.

[23] *Atmega1284P, 8-bit microcontroller*. Rev. 8059D - 11/09. Atmel Corporation. 2009.

List of Figures

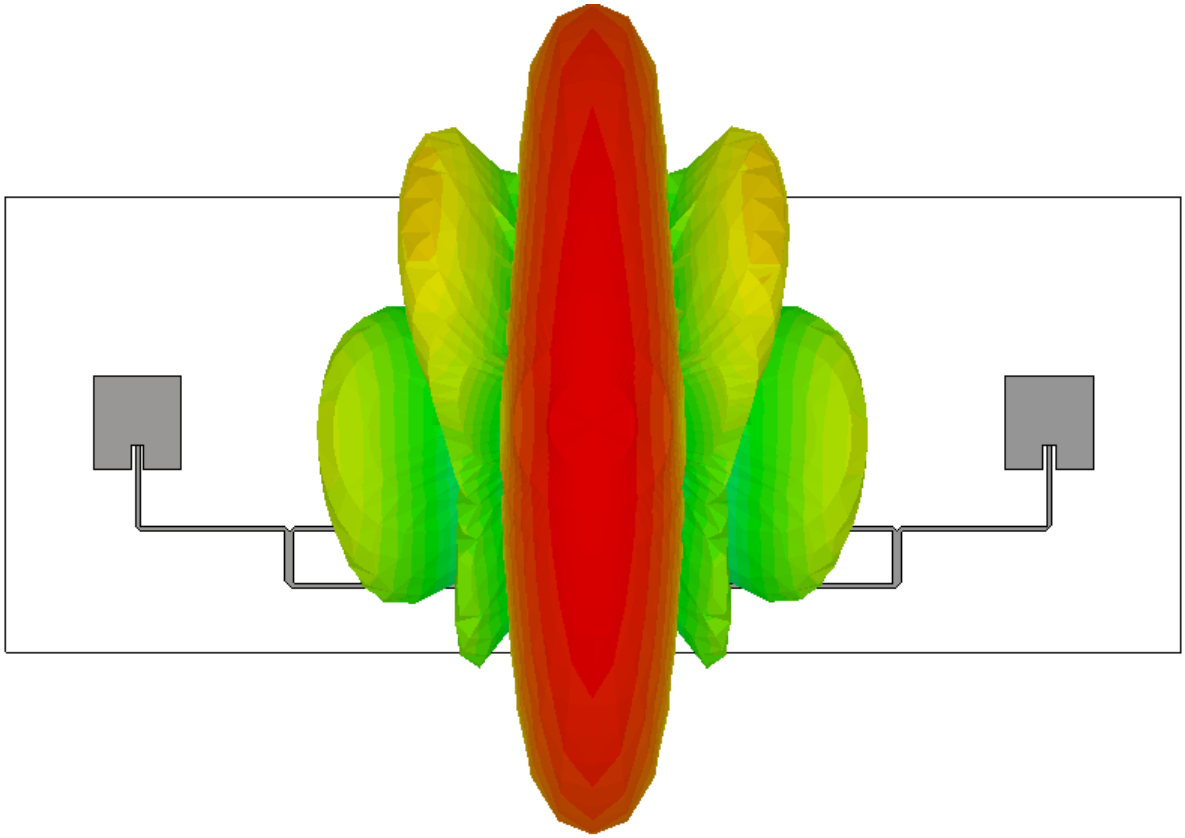

Figure A.1: Three-dimensional far field plot of the antenna front

A Appendix

A.1 Three-dimensional far fields of the antenna

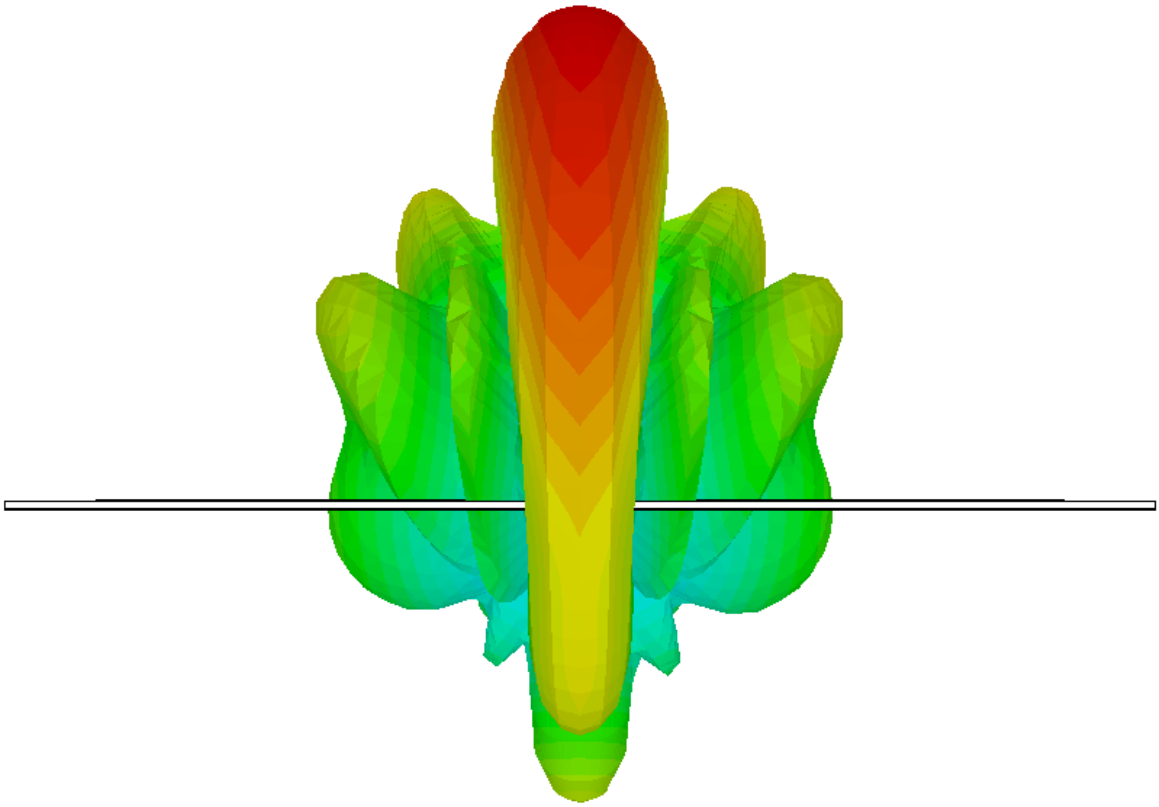

Figure A.2: Three-dimensional far field plot of the antenna bottom

A.2 Antenna characterization signals

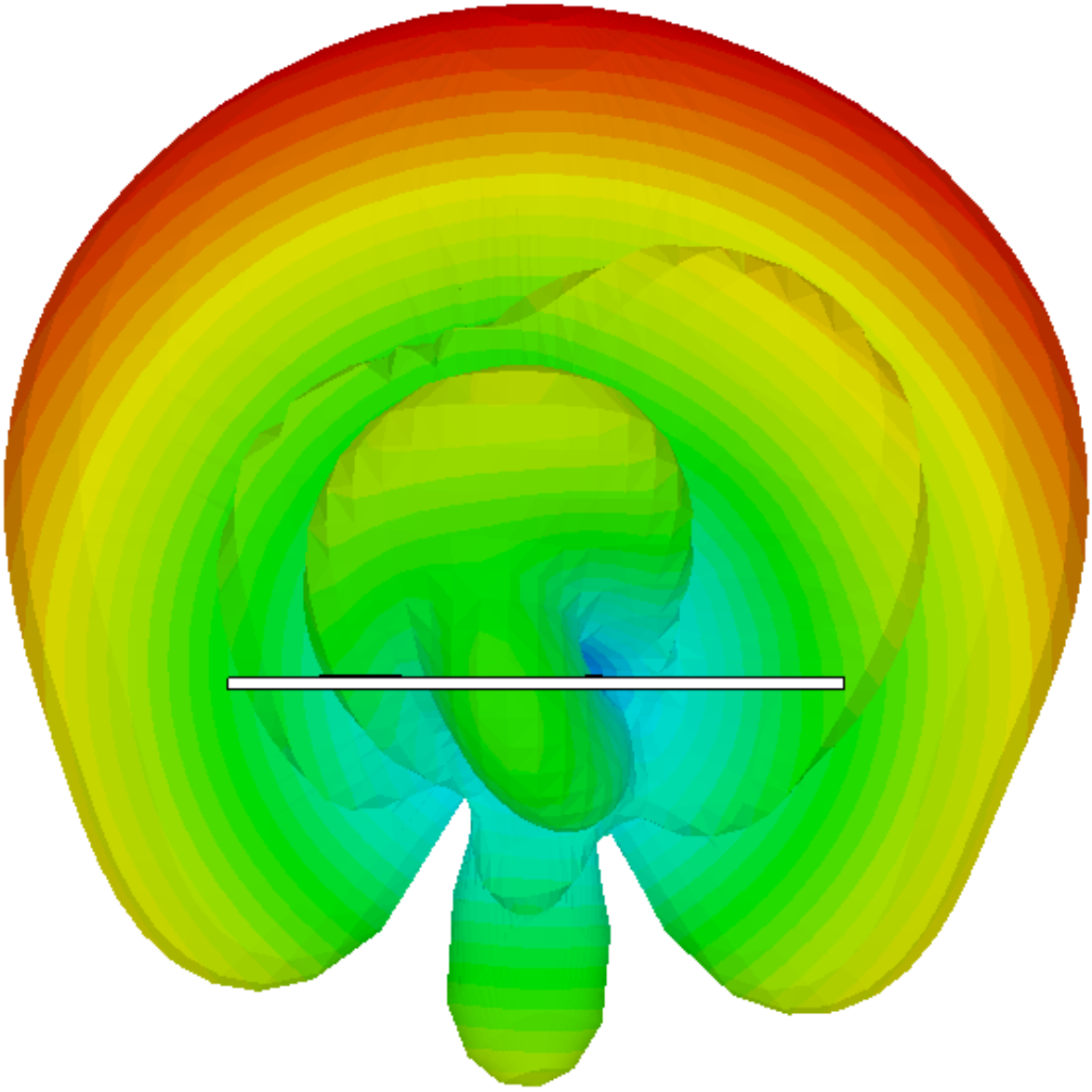

Figure A.3: Three-dimensional far field plot of the antenna side

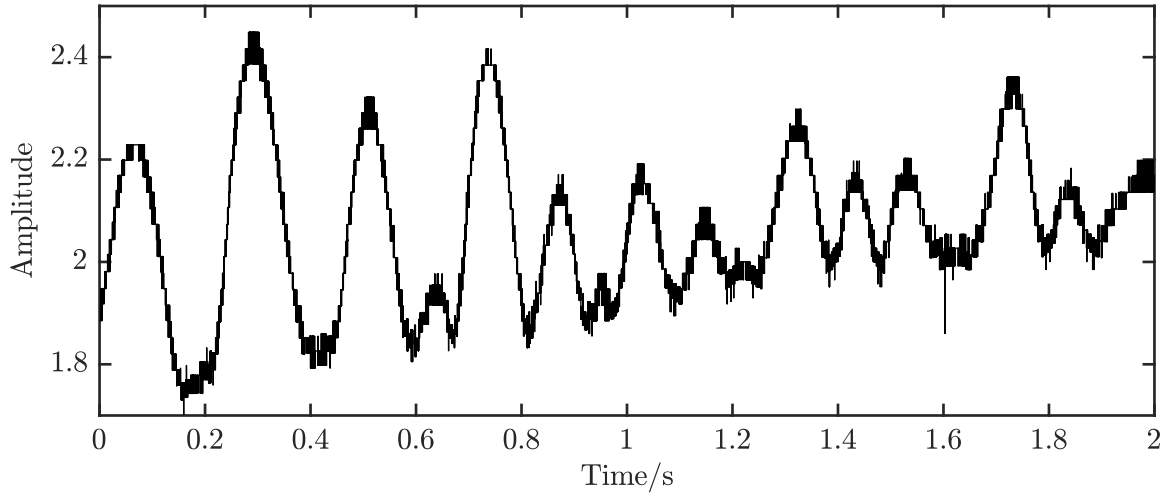

Figure A.4: Signal of antenna characterization in horizontal placement and a tilt angle of 0°

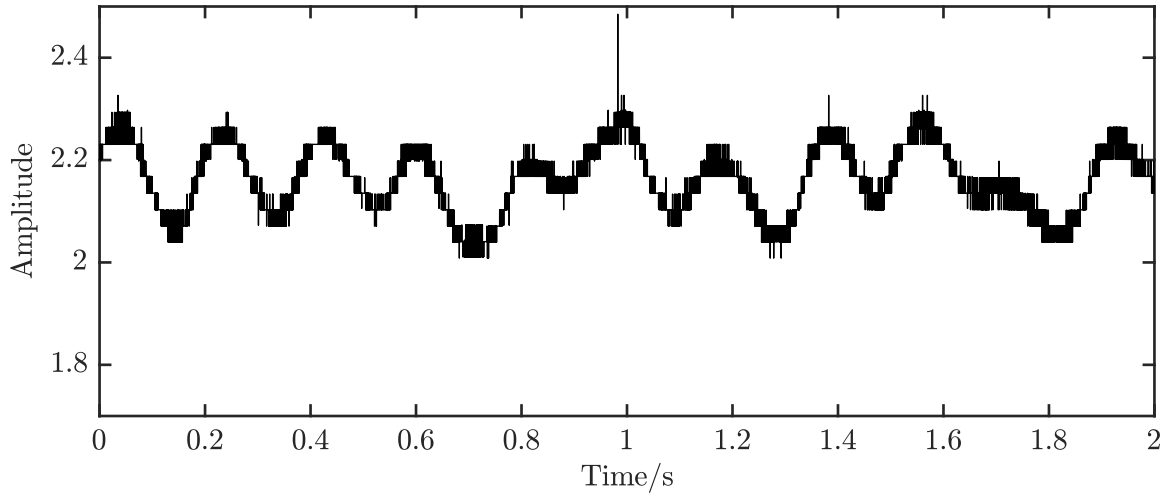

Figure A.5: Signal of antenna characterization in horizontal placement and a tilt angle of 5°

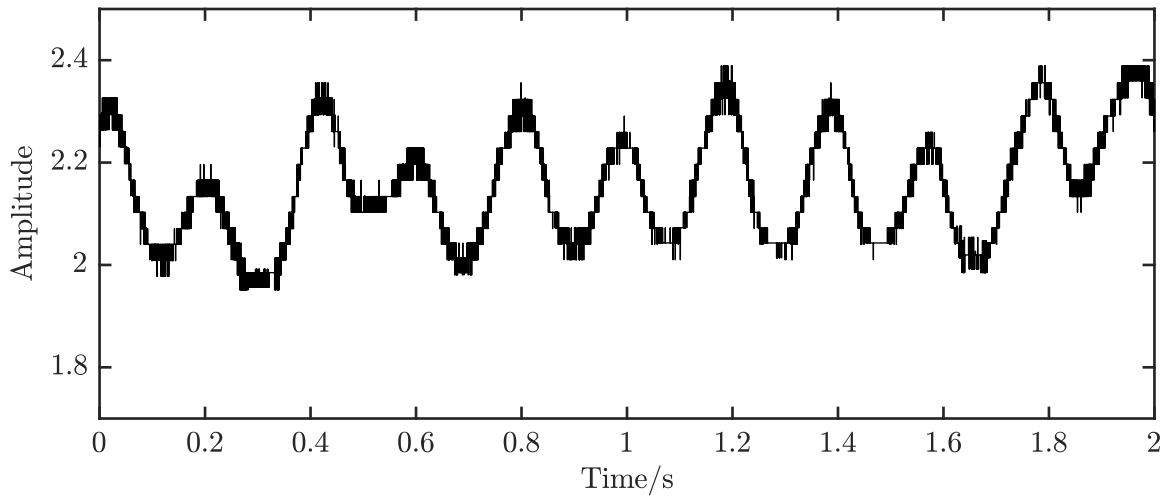

Figure A.6: Signal of antenna characterization in horizontal placement and a tilt angle of -5°

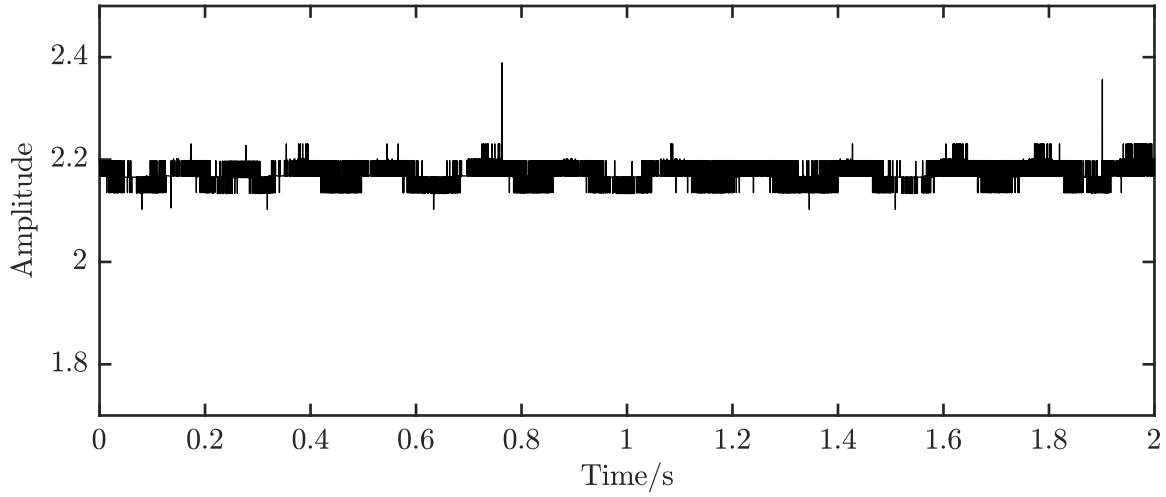

Figure A.7: Signal of antenna characterization in horizontal placement and a tilt angle of 10°

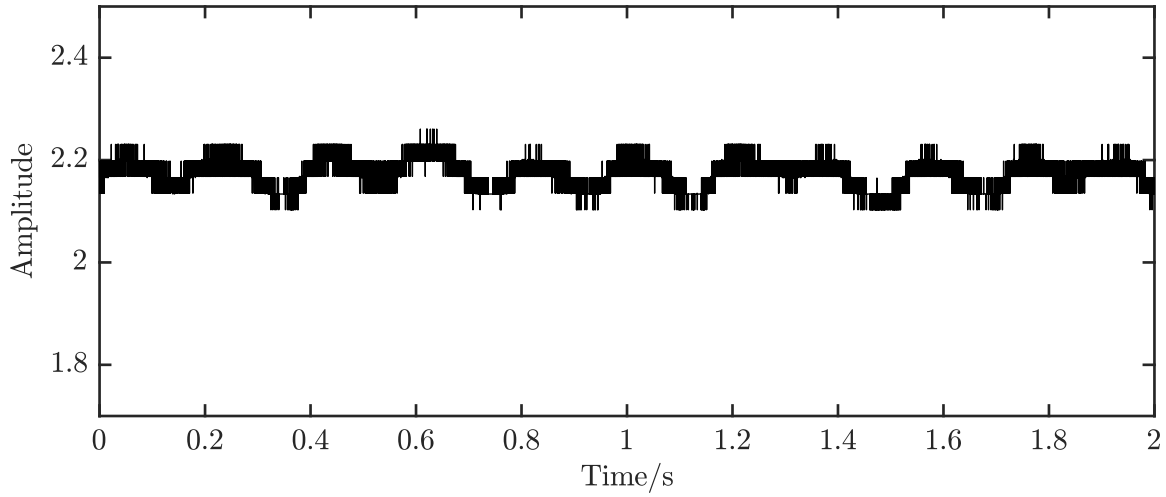

Figure A.8: Signal of antenna characterization in horizontal placement and a tilt angle of -10°

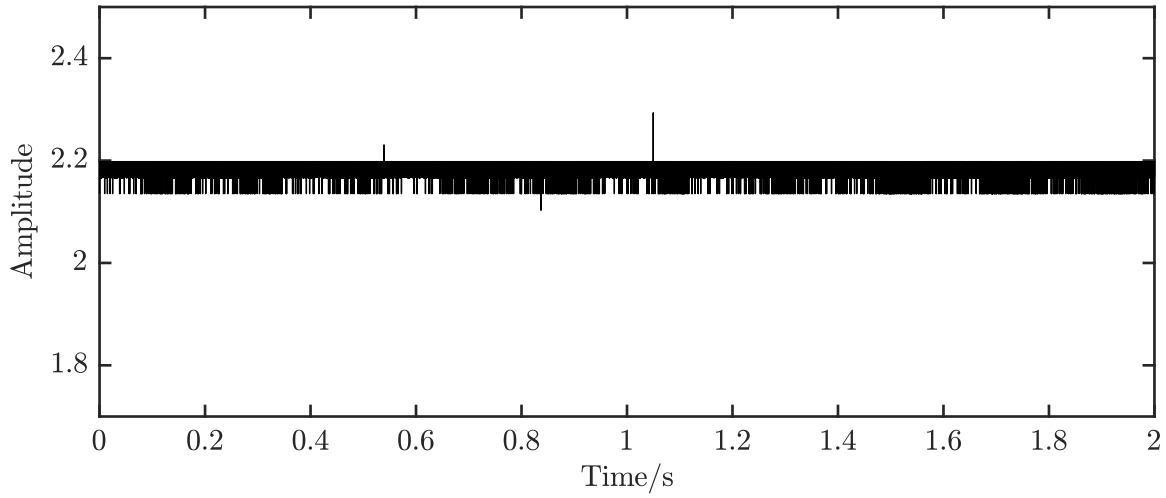

Figure A.9: Signal of antenna characterization in horizontal placement and a tilt angle of 15°

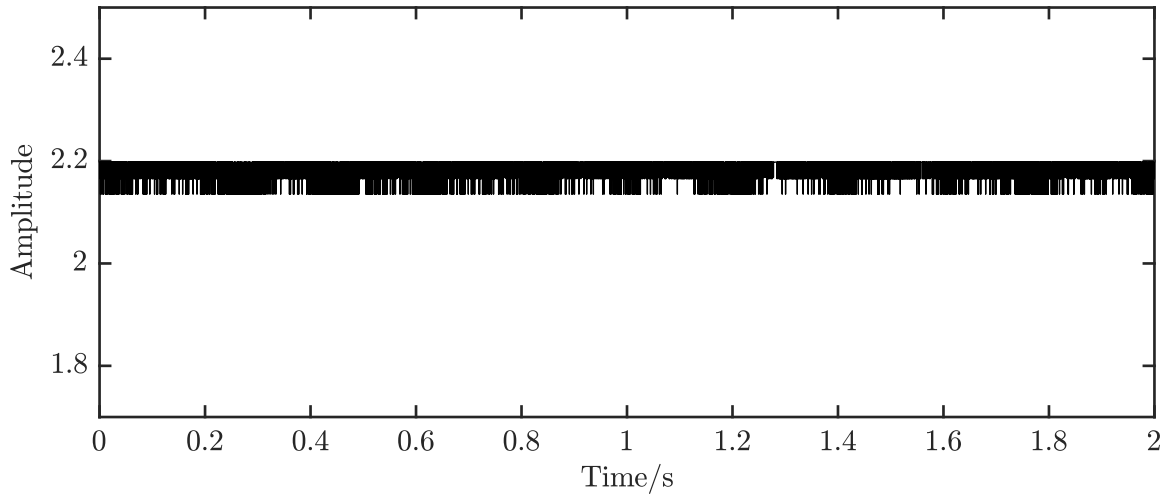

Figure A.10: Signal of antenna characterization in horizontal placement and a tilt angle of -15°

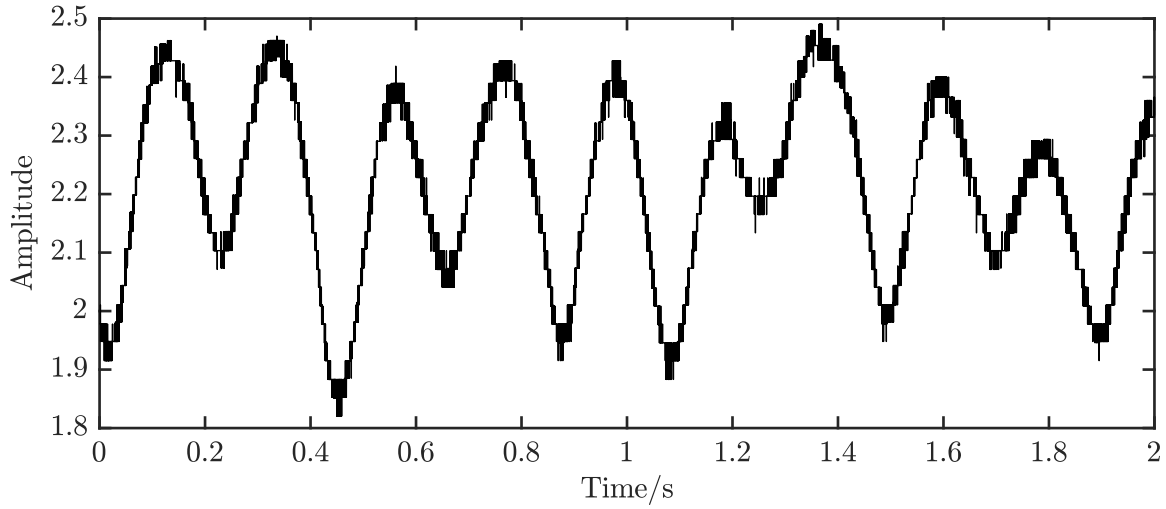

Figure A.11: Signal of antenna characterization in vertical placement and a tilt angle of 0°

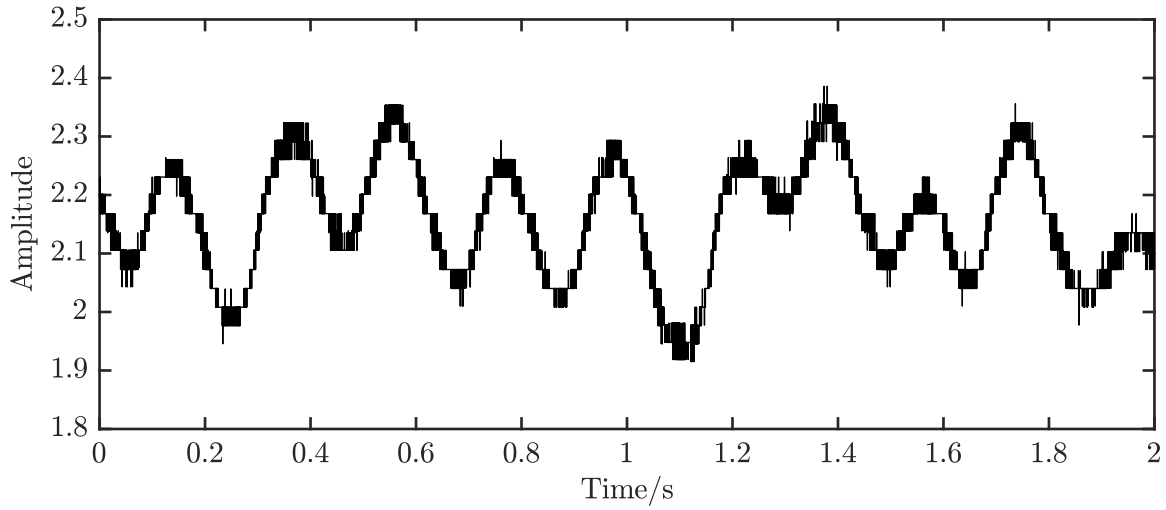

Figure A.12: Signal of antenna characterization in vertical placement and a tilt angle of 80°

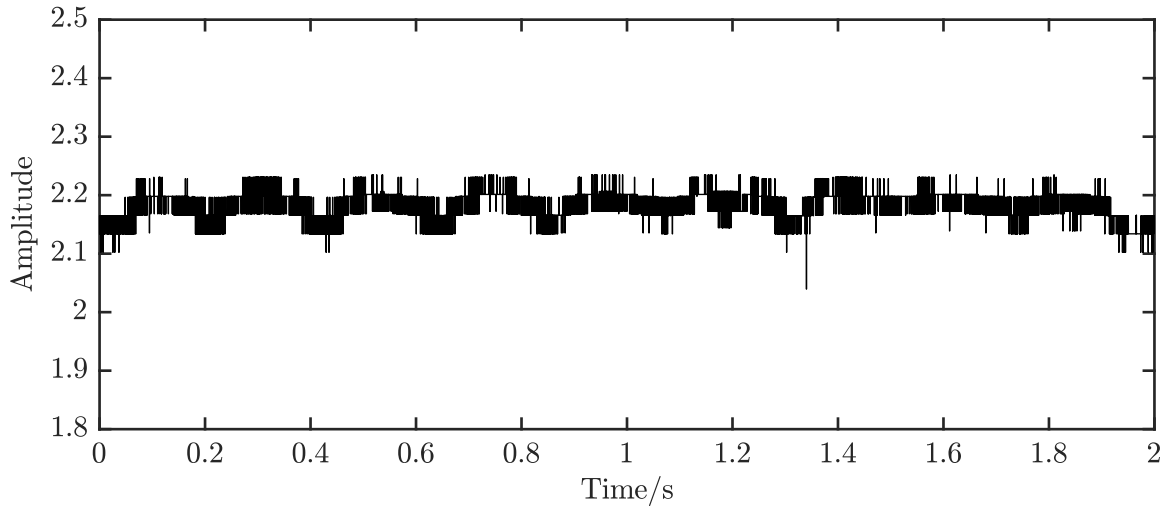

Figure A.13: Signal of antenna characterization in vertical placement and a tilt angle of -80°

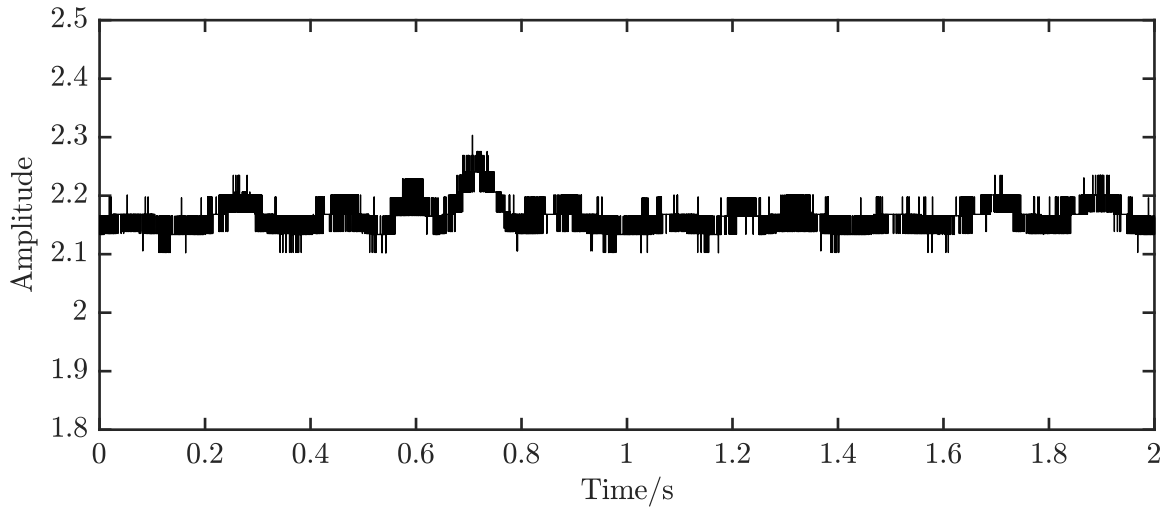

Figure A.14: Signal of antenna characterization in vertical placement and a tilt angle of 90°

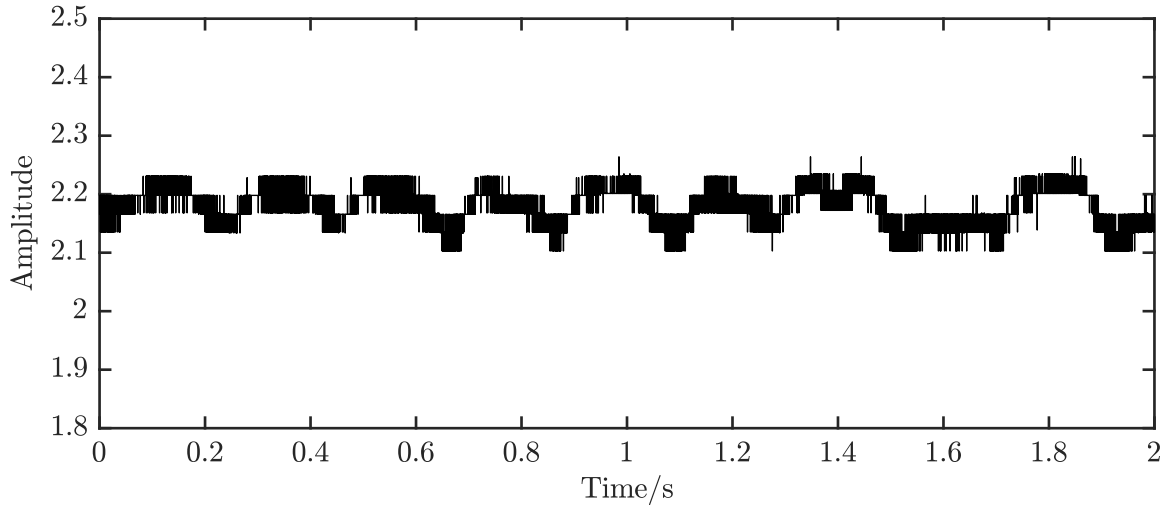

Figure A.15: Signal of antenna characterization in vertical placement and a tilt angle of -90°

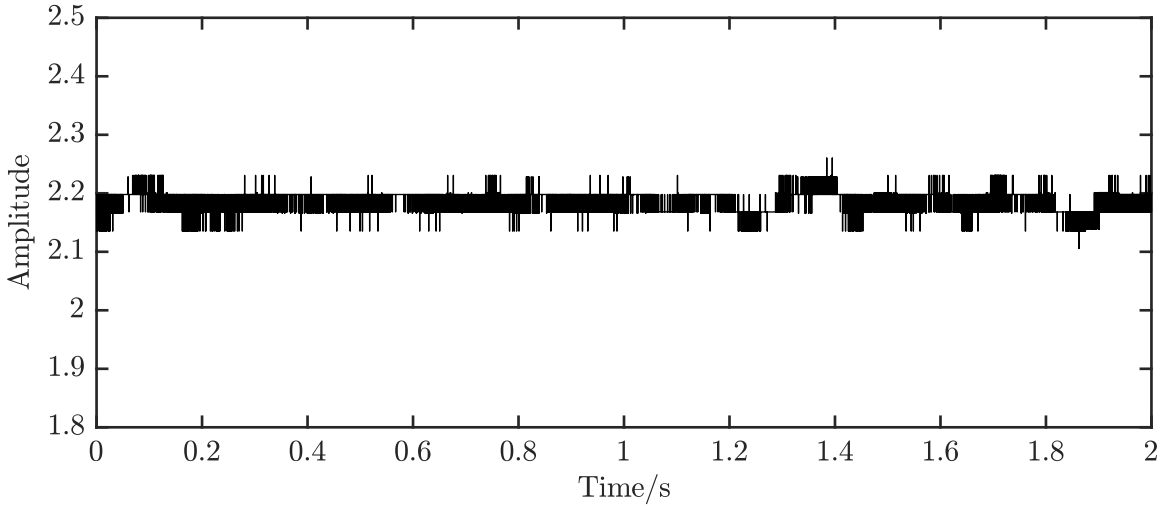

Figure A.16: Signal of antenna characterization in vertical placement and a tilt angle of 100°

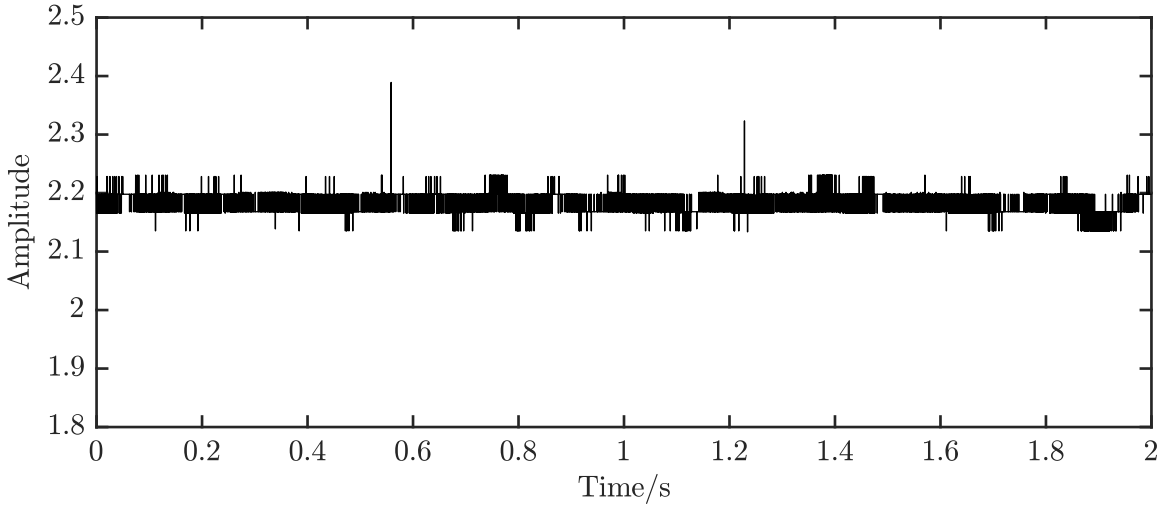

Figure A.17: Signal of antenna characterization in vertical placement and a tilt angle of -100°

A.3 Source Code

```
#define F_CPU 20000000UL  //define Crystal

//include used functions
#include <avr/io.h>
#include <inttypes.h>
#include <stdio.h>
#include <avr/interrupt.h>
#include <stdbool.h>
#include <util/delay.h>
#include "lcdjonasi2c.h"

#define ARRAY_SIZE 300  //define arrays
#define ARRAY_SMALL 30  //define small arrays
#define ALPHA 0.5   //define angle alpha

bool direction = false;     //fmcw ramp direction
bool hold = false;        //fmcw hold ramp
bool hold_next = false;     //fmcw hold next ramp
bool zerostate = false;     //stadard of button
bool cap_load = false;      //load amplify caps
bool radar = false;       //radar on?
bool adc_wait = false;      //adc is waiting
bool adc_read = false;      //start adc read
bool array_filled = false;    //array is filled
bool init_measurment = false; //initialize measurement
bool init_ready = false;    //initializing ready
bool vcc_okay = false;      //vcc voltage in operating range
uint8_t count = 0;        //counter in ISR
uint8_t ramps = 0;        //fmcw numbers of ramps
uint8_t wait_measure = 0;   //waiting counter
uint8_t PREL_T2 = 216;      //preload Timer 2
uint8_t menu = 0;       //lcd menu
uint8_t menu_max = 5;     //how many menus
uint8_t charging = 0;     //count chariging
uint8_t calc = 2;       //factor for bpm calculation
uint8_t counts = 0;       //counter in ISR
uint8_t Byte1=0x00;       //switch/button 1-8 on I2C
uint8_t Byte2=0x00;       //switch/button 9-14 on I2C
uint8_t pwm_value_t0 = 63;    //pwm init value
uint8_t pwm_value_min = 63;   //lower pwm stop
uint8_t pwm_value_max = 92;   //upper pwm stop
uint8_t pwm_value_half = 14;  //middle in pwm range
uint8_t ramp_meas_break = 100;  //fcwm freq. meas. on every x ramps
uint8_t measure_timer = 50;   //wait timer
uint16_t multiplicator = 125; //measure timer*mulitplicator=6250
uint16_t adc_count = 0;     //wait timer
uint16_t vcc_voltage = 0;   //vcc voltage
uint16_t adc_timer = 0;     //wait timer
uint16_t j = 0;         //array position
uint32_t measuredFrequency = 0; //backreaded freq.
int8_t value=0;         //value of rectangular sin / cos
int16_t adc_out = 0;      //readed adc bits
int16_t I_init = 0;       //init value of I low gain
int16_t Q_init = 0;       //init value of Q loq gain
int16_t array[4][ARRAY_SIZE]; //breathing array
int16_t period_2 = ARRAY_SIZE/2;//period for rec. sin / cos
int16_t period_4 = ARRAY_SIZE/4;//periode for rec. sin / cos
int16_t period_3_4 = 3*ARRAY_SIZE;//periode for rec. sin / cos
float phase_array[2][ARRAY_SIZE];//phase of breathing
float output[2][ARRAY_SMALL]; //calculated sfa output
float maxValue[2];        //highest freq.
float maxValues[2];       //highest output

void setup_pins()
{
  //setup pins according to circuit diagram v1
```

```
67    DDRA &= ~((1<<2)|(1<<3)|(1<<5)|(1<<6));
68    DDRB |= (1<<0)|(1<<2)|(1<<4);
69    DDRB &= ~(1<<1);
70    DDRC |= (1<<3)|(1<<4)|(1<<5);
71    DDRD |= (1<<0)|(1<<1)|(1<<3);
72    DDRD &= ~(1<<2);
73    PORTD |= (1<<3);
74  }
75
76  void setupPWM() {
77    //setup timer 0 for PWM at OUT OCR0B
78    TCCR0A |= (1 << COM0B1) | (1 << WGM01) | (1 << WGM00);
79    TCCR0B |= (1 << CS00);
80    OCR0B = pwm_value_t0;
81  }
82
83  void setupTimer1() {
84    //setup timer 1 for external clock
85    TCCR1B = (1 << CS12) | (1 << CS11);
86    TIMSK1 = 0;
87  }
88
89  void setupTimer2() {
90    //setup Timer2 for 160us
91    TCCR2B |= (1 << CS22)|(1<<CS20);
92    TCNT2 = 231;
93    TIMSK2 |= (1<<TOIE2);
94  }
95
96  void setup_ADC()
97  {
98    //setup adc with AVCC as reference
99    ADMUX |= (1<<REFS0);
100   ADCSRA |= (1<<ADATE)|(1<<ADPS2)|(1<<ADPS1)|(1<<ADEN);
101 }
102
103 void read_buttons()
104 {
105   i2c_start(0x81);    //start I2C communication to 0x81
106   Byte1 = i2c_readAck();  //read I2C
107   Byte2 = i2c_readNak();  //read I2C
108   i2c_stop();       //stop I2C communicaiton
109 }
110
111 void start_radar()
112 {
113   PORTC |= ((1<<3));      //enable 3.3V
114   PORTB |= (1<<0);      //2.5V for amplifiers
115   PORTC |= (1<<4)|(1<<5);   //charge amplify caps
116   PORTD |= (1<<0)|(1<<1);   //charge amplify caps
117   charging = 0;       //charger count 0
118   cap_load = true;      //caps are loading
119   PORTB |= (1<<2);      //turn radar on
120   radar = true;       //RADAR ON
121 }
122
123 void stop_radar()
124 {
125   OCR0B = 0;          //no freq. modulation
126   PORTB &= ~(1<<2);     //turn radar off
127   PORTB &= ~(1<<0);     //turn 2.5V for amplifiers off
128   PORTC &= ~((1<<3));     //disable 3.3V
129   radar = false;        //RADAR OFF
130 }
131
132 uint16_t read_vcc()
133 {
134   //read Vcc voltage - Pin A7 - ADC7: ADMUX 00111
135   ADMUX |= (1<<MUX2)|(1<<MUX1)|(1<<MUX0);
```

```
136   ADMUX &= ~((1<<MUX4)|(1<<MUX3)|(1<<MUX1));
137   while (adc_count <= 20000){adc_count++;}
138   adc_count = 0;
139   ADCSRA |= (1<<ADSC);
140   adc_out = ADCL+(ADCH<<8);
141   return vcc_voltage;
142 }
143
144 int16_t read_LowGain_I()
145 {
146   //read I-Value LOW Gain - Pin A5 - ADC5: ADMUX 00101
147   ADMUX |= (1<<MUX2)|(1<<MUX0);
148   ADMUX &= ~((1<<MUX4)|(1<<MUX3)|(1<<MUX1));
149   while (adc_count <= 20000){adc_count++;}
150   adc_count = 0;
151   ADCSRA |= (1<<ADSC);
152   adc_out = ADCL+(ADCH<<8);
153   return adc_out;
154 }
155 int16_t read_LowGain_Q()
156 {
157   //read Q-Value LOW Gain - Pin A3 - ADC3: ADMUX 00011
158   ADMUX |= (1<<MUX1)|(1<<MUX0);
159   ADMUX &= ~((1<<MUX4)|(1<<MUX3)|(1<<MUX2));
160   while (adc_count <= 20000){adc_count++;}
161   adc_count = 0;
162   ADCSRA |= (1<<ADSC);
163   adc_out = ADCL+(ADCH<<8);
164   return adc_out;
165 }
166 int16_t read_HighGain_I()
167 {
168   //read I-Value HIGH Gain - Pin A6 - ADC6: ADMUX 00110
169   ADMUX |= (1<<MUX2)|(1<<MUX1);
170   ADMUX &= ~((1<<MUX4)|(1<<MUX3)|(1<<MUX0));
171   while (adc_count <= 20000){adc_count++;}
172   adc_count = 0;
173   ADCSRA |= (1<<ADSC);
174   adc_out = ADCL+(ADCH<<8);
175   return adc_out;
176 }
177 int16_t read_HighGain_Q()
178 {
179   //read Q-Value HIGH Gain - Pin A2 - ADC2: ADMUX 00010
180   ADMUX |= (1<<MUX1);
181   ADMUX &= ~((1<<MUX4)|(1<<MUX3)|(1<<MUX2)|(1<<MUX0));
182   while (adc_count <= 20000){adc_count++;}
183   adc_count = 0;
184   ADCSRA |= (1<<ADSC);
185   adc_out = ADCL+(ADCH<<8);
186   return adc_out;
187 }
188
189 ISR(TIMER2_OVF_vect)
190 {
191   TCNT2 = 231;
192   //init low gain values
193   if (init_measurment == true)
194   {
195     adc_timer++;
196     if (adc_timer <= 36250)
197     {
198       I_init = read_LowGain_I();
199       Q_init = read_HighGain_Q();
200       init_ready = true;
201       adc_timer = 0;
202     }
203     if (init_ready == true)
204     {
```

```
205       start_radar();
206       adc_read = true;
207     }
208   }
209   //read adc in array
210   if (adc_read == true)
211   {
212     adc_timer++;
213     if (adc_timer >= 250)
214     {
215       array[0][j] = read_LowGain_I();
216       array[1][j] = read_LowGain_Q();
217       array[2][j] = read_HighGain_I();
218       array[3][j] = read_HighGain_Q();
219       j++;
220       if (j>=ARRAY_SIZE)
221       {
222         array_filled = true;
223         adc_read = false;
224       }
225       adc_timer = 0;
226     }
227   }
228   //charge amplify caps
229   if (cap_load==true)
230   {
231     charging++;
232     if (charging >= 100)
233     {
234       PORTC &= ~(1<<4);
235       PORTD &= ~(1<<0);
236     }
237     if (charging >= 200)
238     {
239       PORTC &= ~(1<<5);
240       PORTD &= ~(1<<1);
241       cap_load = false;
242     }
243   }
244   //measure cw freq. and adjust to operating freq.
245   if ((menu == 2) || (menu == 3))
246   {
247     OCR0B = 75;
248     wait_measure++;
249     if (wait_measure >= measure_timer)
250     {
251       TCCR1B &= ~((1<<CS12) | (1<<CS11));
252       measuredFrequency = TCNT1;
253       if (measuredFrequency > 23560)
254       {
255         OCR0B--;
256       }
257       if (measuredFrequency < 23558)
258       {
259         OCR0B++;
260       }
261       TCNT1 = 0;
262       TCCR1B |= (1 << CS12) | (1 << CS11);
263       wait_measure = 0;
264     }
265   }
266   //measure fmcw freq. via holding the ramp and adjust to operating freq.
267   if (menu == 4)
268   {
269     if (hold == false)
270     {
271       if (direction == false)
272       {
273         pwm_value_t0++;
```

```
274         if (hold_next == true)
275         {
276           count++;
277           if (count >= pwm_value_half && hold_next == true)
278           {
279             TCCR1B |= (1 << CS12) | (1 << CS11);
280             wait_measure = 0;
281             hold = true;
282           }
283         }
284         if (pwm_value_t0 == (pwm_value_max+1))
285         {
286           direction = true;
287         }
288       }
289       if (direction == true)
290       {
291         pwm_value_t0--;
292         if (pwm_value_t0 == pwm_value_min)
293         {
294           direction = false;
295           ramps++;
296           if (ramps >= ramp_meas_break)
297           {
298             hold_next = true;
299           }
300
301         }
302       }
303       // block voltage over 3.3V
304       if (pwm_value_t0 >= 158)
305       {
306         pwm_value_t0 = 157;
307       }
308     }
309     if (hold == true)
310     {
311       wait_measure++;
312       if (wait_measure >= measure_timer)
313       {
314         TCCR1B &= ~((1<<CS12) | (1<<CS11));
315         hold_next = false;
316         ramps = 0;
317         count = 0;
318         measuredFrequency = TCNT1;
319         if (measuredFrequency > 23560)
320         {
321           pwm_value_min--;
322           pwm_value_max--;
323           pwm_value_half--;
324         }
325         if (measuredFrequency < 23558)
326         {
327           pwm_value_min++;
328           pwm_value_max++;
329           pwm_value_half++;
330         }
331         TCNT1 = 0;
332         hold = false;
333       }
334     }
335     OCR0B = pwm_value_t0;
336   }
337 }
338
339 //substract offset from raw values and calculate the phase to an continious
      signal
340 void offsetPHASE(int16_t array[][ARRAY_SIZE], uint16_t size, int16_t I_offset,
      int16_t Q_offset)
341 {
342   float Vold = 0;
```

```
343   float Vnew = 0;
344   float diff = 0;
345   bool newdiff = true;
346 
347   for (uint16_t k = 0; k < size; k++)
348   {
349     array[0][k] = array[0][k] - I_offset;
350     array[1][k] = array[1][k] - Q_offset;
351     array[2][k] = array[2][k] - 512;
352     array[3][k] = array[3][k] - 512;
353   }
354   for (uint16_t k = 0; k < size; k++)
355   {
356     phase_array[0][k] = atan2(array[0][k],array[1][k]);
357     phase_array[1][k] = atan2(array[2][k],array[3][k]);
358   }
359   for (uint16_t n=0; n < 2; n++)
360   {
361     for (uint16_t k = 0; k < size-1; k++)
362     {
363       Vold = phase_array[n][k];
364       Vnew = phase_array[n][k+1];
365       if (((Vnew-Vold) >= -2) && ((Vnew-Vold) <= 2))
366         {newdiff = true;}
367       if ((newdiff==true) && (((Vnew-Vold) < -2) || ((Vnew-Vold) > 2)))
368       {
369         diff = fabs(Vold);
370         newdiff = false;
371       }
372       if ((Vnew-Vold) < -2)
373         {phase_array[n][k+1] = Vnew + (2*-diff);}
374       if ((Vnew-Vold) > 2)
375         {phase_array[n][k+1] = Vnew + (2*-diff);}
376     }
377   }
378 }
379 //remove the average from the phase
380 void mittelwertFilter(float phase_array[][ARRAY_SIZE], uint16_t size)
381 {
382   float mittelwert = 0.0;
383   for (uint16_t n = 0; n < 2; n++){
384     mittelwert = 0;
385     for (uint16_t i = 0; i < size; i++)
386       {mittelwert += phase_array[n][i];}
387     mittelwert /= size;
388     for (uint16_t i = 0; i < size; i++)
389       {phase_array[n][i] -= mittelwert;}
390   }
391 }
392 //create a binary cosine
393 int16_t cos_rec(int16_t angle)
394 {
395   if ((angle <= period_4)||(angle>period_3_4)) value = 1;
396   else value =-1;
397   return value;
398 }
399 //create a binary sine
400 int16_t sin_rec(int16_t angle)
401 {
402   if (angle > period_2) value= -1;
403   else value = 1;
404   return value;
405 }
406 //perform a simple frequency analysis
407 void SFA(float phase_array[][ARRAY_SIZE], uint16_t size)
408 {
409   int32_t sumReal = 0;
410   int32_t sumImag = 0;
411   uint16_t angle = 0;
```

```
412   for (uint16_t i = 0; i < 2; i++){
413     for (uint16_t k = 0; k < size; k++) {
414       sumReal = 0;
415       sumImag = 0;
416       angle = 0;
417       for (uint16_t n = 0; n < size; n++) {
418         if(angle > size) angle -= size;
419         sumReal += phase_array[i][n] * cos_rec(angle);
420         sumImag += phase_array[i][n] * sin_rec(angle);
421         angle += k;
422       }
423       output[i][k] = (sqrt(pow(sumReal, 2) + pow(sumImag, 2))) / 64;
424     }
425   }
426 }
427 //find the highest peak in the sfa and its position
428 void filterHighestValues(float array[][ARRAY_SMALL], uint16_t size, float*
      maxPositions)
429 {
430   for (uint8_t i = 0; i < 2; i++)
431   {
432     maxValue[i] = 0;
433     float maxPosition = 0;
434     for (uint16_t j = 5; j < size-1; j++)
435     {
436       if (array[i][j] > maxValue[i])
437       {
438         maxValue[i] = array[i][j];
439         maxPosition = j;
440       }
441     }
442     if (maxValue[0]>10)
443       {maxPositions[0] = (float)maxPosition*calc;}
444     else
445       {maxPositions[0]=0;}
446     if (maxValue[1]>120)
447       {maxPositions[1] = (float)maxPosition*calc;}
448     else
449       {maxPositions[1]=0;}
450   }
451
452 }
453
454 int main(void)
455 {
456     setup_pins();      //perform pin setup
457   lcd_st7032_init_i2c();  //initialzie I2C
458   lcd_st7032_init();     //initialize LCD
459   lcd_st7032_clear();    //clear LCD
460   setupPWM();        //perfrom PWM setup
461   setupTimer1();       //setup timer 1
462   setupTimer2();       //setup timer 2
463   setup_ADC();       //perform adc setup
464   sei();           //enable interrupts
465   while (1)
466     {
467     //check the vcc voltage and allow funtion between 9 and 16V
468     vcc_voltage = read_vcc();
469     if ((vcc_voltage >= 332) && (vcc_voltage <= 590))
470       {vcc_okay = true;}
471     else
472       {vcc_okay = false;}
473     //read the button and switches and perform menu navigation
474     read_buttons();
475     if ((Byte1 & (1<<0)) && zerostate)
476     {
477       lcd_st7032_clear();
478       menu++;
479       zerostate = 0;
```

```
480       if (menu >= menu_max)
481         {menu = 0;}
482     }
483     if ((Byte1 & (1<<1)) && zerostate)
484     {
485       lcd_st7032_clear();
486       menu--;
487       zerostate = 0;
488       if (menu >= menu_max)
489         {menu = menu_max-1;}
490     }
491     if (((Byte1 & (1<<0)) || (Byte1 & (1<<1))) == 0)
492       {zerostate = 1;}
493     //first menu - start screen
494     if (menu == 0)
495     {
496       if (radar==true)
497         {stop_radar();}
498       lcd_st7032_set_cursor(0,0);
499       lcd_st7032_print("SYSTEM: OFF");
500       lcd_st7032_set_cursor(1,0);
501       lcd_st7032_print("RADAR: OFF");
502     }
503     //second menu - radar ic on, radar transmitting off
504     if (menu == 1)
505     {
506       PORTC |= ((1<<3));
507       PORTB &= ~(1<<2);
508       lcd_st7032_set_cursor(0,0);
509       lcd_st7032_print("SYSTEM: ON");
510       lcd_st7032_set_cursor(1,0);
511       lcd_st7032_print("RADAR: OFF");
512     }
513     //third menu - cw funtion with backreaded freq. on screen
514     if ((menu == 2) && (vcc_okay == true))
515     {
516       if (radar==false)
517         {start_radar();}
518       lcd_st7032_set_cursor(0,0);
519       lcd_st7032_print("[CW] Freqency: ");
520       lcd_st7032_set_cursor(1,0);
521       lcd_st7032_print2(measuredFrequency);
522       lcd_st7032_set_cursor(1,8);
523       lcd_st7032_print2(OCR0B);
524     }
525     //fourth menu - cw measurement to extract respiration rate
526     if ((menu == 3) && (vcc_okay == true))
527     {
528       if ((radar == false) && (array_filled == false))
529         {start_radar();}
530       if ((Byte2 & (1<<5)) != 0)
531       {
532         stop_radar();
533         PORTC |= ((1<<3));
534         lcd_st7032_set_cursor(0,0);
535         lcd_st7032_print("INITIALIZING... ");
536         init_measurment = true;
537       }
538       if ((array_filled == false) && (adc_read == true))
539       {
540         init_measurment = false;
541         lcd_st7032_set_cursor(0,0);
542         lcd_st7032_print("READ DATA...    ");
543         lcd_st7032_set_cursor(1,12);
544         lcd_st7032_print_U16(j);
545       }
546       if ((array_filled == true))
547       {
```

```
548         lcd_st7032_set_cursor(0,0);
549         lcd_st7032_print("PROCESSING...    ");
550         adc_read = false;
551         stop_radar();
552         offsetPHASE(array, ARRAY_SIZE,I_init,Q_init);
553         mittelwertFilter(phase_array, ARRAY_SIZE);
554         SFA(phase_array, ARRAY_SIZE);
555         filterHighestValues(output, ARRAY_SMALL, maxValues);
556         lcd_st7032_clear();
557         lcd_st7032_set_cursor(0,0);
558         lcd_st7032_print("RESULTS...      ");
559         if (((maxValues[0] >= 12) && (maxValues[0] <= 40)) || ((maxValues[1] >=
                12) && (maxValues[1] <= 40)))
560         {
561           lcd_st7032_set_cursor(1,0);
562           lcd_st7032_print("BREATHING: YES  ");
563         }
564         else
565         {
566           lcd_st7032_set_cursor(1,0);
567           lcd_st7032_print("BREATHING: NO   ");
568         }
569         _delay_ms(3000);
570         lcd_st7032_set_cursor(1,0);
571         lcd_st7032_print("                ");
572         lcd_st7032_set_cursor(1,0);
573         lcd_st7032_print_d(maxValues[0]);
574         lcd_st7032_set_cursor(1,8);
575         lcd_st7032_print_d(maxValues[1]);
576         _delay_ms(5000);
577         j = 0;
578         start_radar();
579         array_filled = false;
580       }
581       if (((Byte2 & (1<<5)) == 0) && (adc_read == false) && (array_filled ==
              false))
582       {
583         lcd_st7032_set_cursor(0,0);
584         lcd_st7032_print("[CW] measurement");
585         lcd_st7032_set_cursor(1,0);
586         lcd_st7032_print("                ");
587       }
588     }
589     //fifth menu - fmcw function with backreaded freq. on screen
590     if ((menu == 4) && (vcc_okay == true))
591     {
592       if (radar==false)
593         {start_radar();}
594       lcd_st7032_set_cursor(0,0);
595       lcd_st7032_print("[FMCW]Freqency:");
596       lcd_st7032_set_cursor(1,0);
597       lcd_st7032_print2(measuredFrequency);
598     }
599     //block cw/fmcw funtion if vcc out of range
600     if (((menu == 2) || (menu == 3) || (menu == 4)) && (vcc_okay == false))
601     {
602       stop_radar();
603       lcd_st7032_set_cursor(0,0);
604       lcd_st7032_print("VCC out of Range");
605       lcd_st7032_set_cursor(1,0);
606       lcd_st7032_print("No function!    ");
607     }
608   }
609 }
```

A.4 Circuit diagram

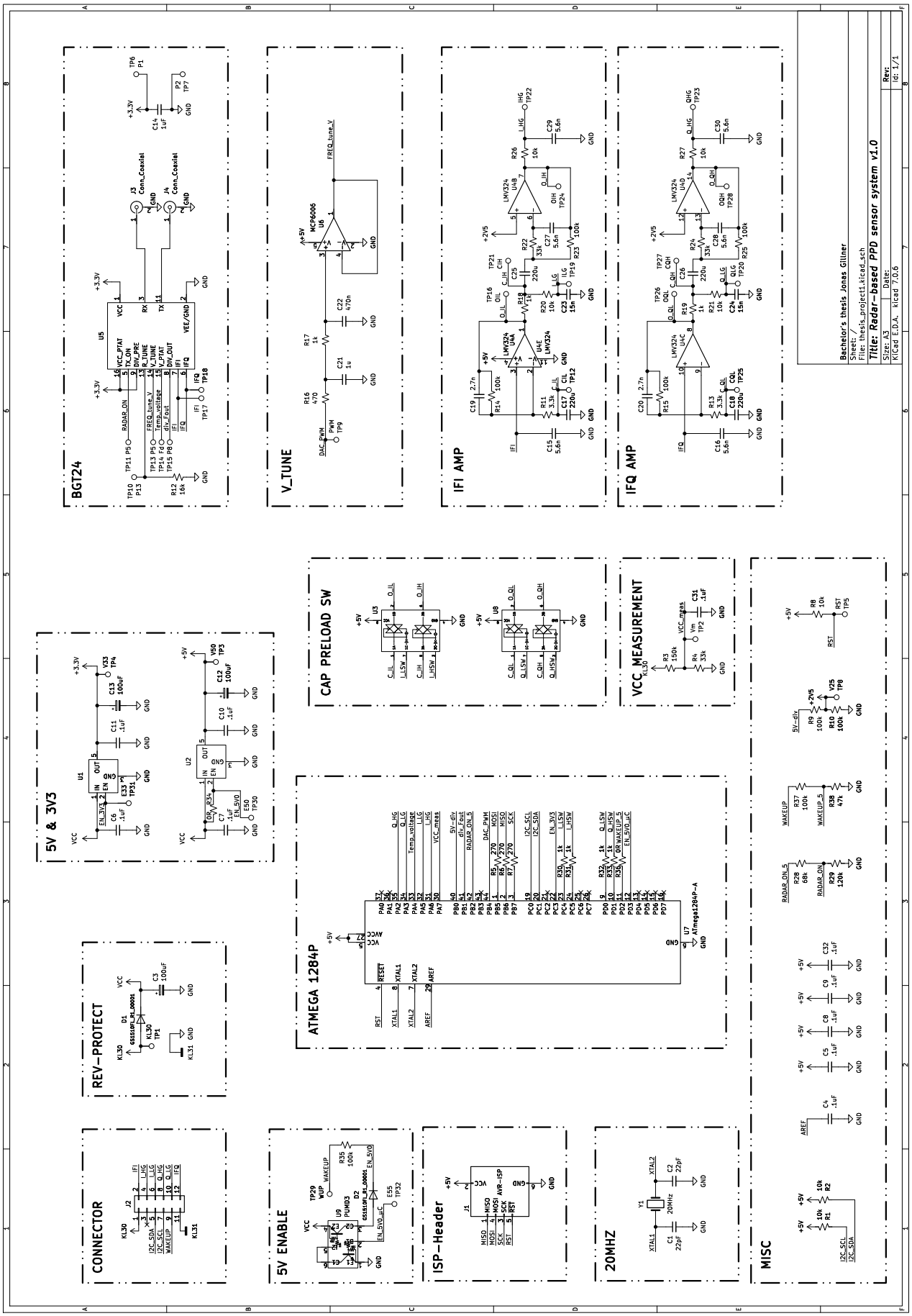

Figure A.18: Circuit diagram of the developed radar-based sensor system